



## Unidirectional frequency conversion in microring resonators for on-chip frequency-multiplexed single-photon sources

Heuck, Mikkel; Koefoed, Jacob Gade; Christensen, Jesper Bjerger; Ding, Yunhong; Frandsen, Lars Hagedorn; Rottwitt, Karsten; Oxenløwe, Leif Katsuo

*Published in:*  
New Journal of Physics

*Link to article, DOI:*  
[10.1088/1367-2630/ab09a7](https://doi.org/10.1088/1367-2630/ab09a7)

*Publication date:*  
2019

*Document Version*  
Publisher's PDF, also known as Version of record

[Link back to DTU Orbit](#)

*Citation (APA):*  
Heuck, M., Koefoed, J. G., Christensen, J. B., Ding, Y., Frandsen, L. H., Rottwitt, K., & Oxenløwe, L. K. (2019). Unidirectional frequency conversion in microring resonators for on-chip frequency-multiplexed single-photon sources. *New Journal of Physics*, 21(3), [033037]. <https://doi.org/10.1088/1367-2630/ab09a7>

---

### General rights

Copyright and moral rights for the publications made accessible in the public portal are retained by the authors and/or other copyright owners and it is a condition of accessing publications that users recognise and abide by the legal requirements associated with these rights.

- Users may download and print one copy of any publication from the public portal for the purpose of private study or research.
- You may not further distribute the material or use it for any profit-making activity or commercial gain
- You may freely distribute the URL identifying the publication in the public portal

If you believe that this document breaches copyright please contact us providing details, and we will remove access to the work immediately and investigate your claim.

PAPER • OPEN ACCESS

## Unidirectional frequency conversion in microring resonators for on-chip frequency-multiplexed single-photon sources

To cite this article: Mikkel Heuck *et al* 2019 *New J. Phys.* **21** 033037

View the [article online](#) for updates and enhancements.



**IOP** ebooks™

Bringing you innovative digital publishing with leading voices to create your essential collection of books in STEM research.

Start exploring the collection - download the first chapter of every title for free.



## PAPER

## Unidirectional frequency conversion in microring resonators for on-chip frequency-multiplexed single-photon sources

## OPEN ACCESS

## RECEIVED

15 October 2018

## REVISED

29 January 2019

## ACCEPTED FOR PUBLICATION

22 February 2019



## PUBLISHED

28 March 2019

Original content from this work may be used under the terms of the [Creative Commons Attribution 3.0 licence](https://creativecommons.org/licenses/by/4.0/).

Any further distribution of this work must maintain attribution to the author(s) and the title of the work, journal citation and DOI.



Mikkel Heuck , Jacob Gade Koefoed , Jesper Bjerger Christensen, Yunhong Ding, Lars Hagedorn Frandsen, Karsten Rottwitt and Leif Katsuo Oxenløwe

Department of Photonics Engineering, Technical University of Denmark, Building 343, DK-2800 Kgs. Lyngby, Denmark

E-mail: [mrheuck@gmail.com](mailto:mrheuck@gmail.com)

**Keywords:** single photon source, quantum information technology, frequency conversion

## Abstract

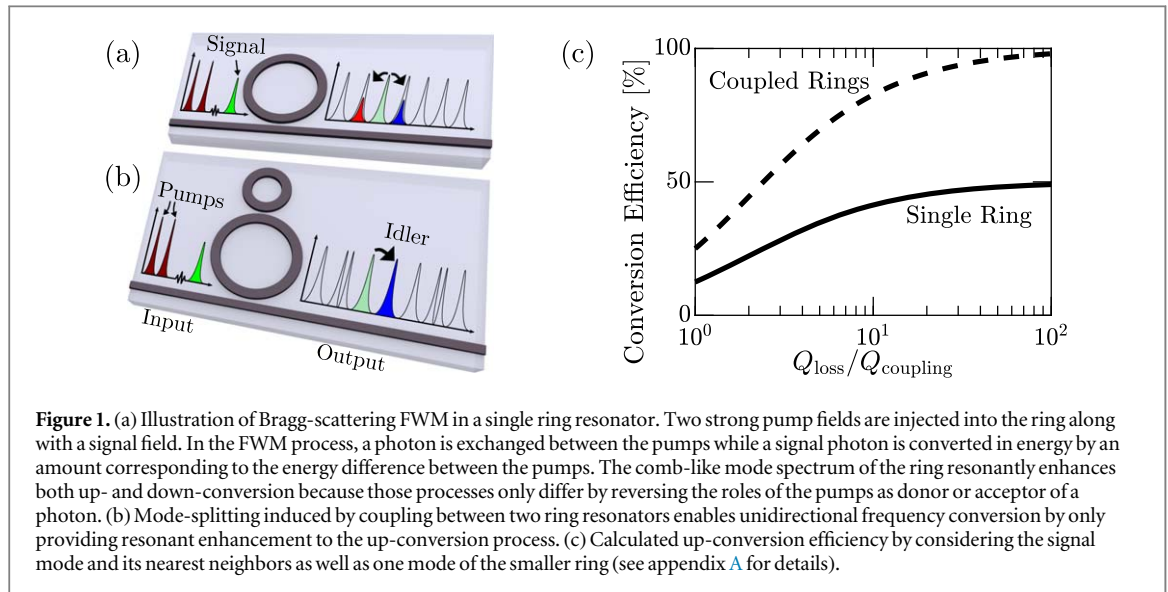
Microring resonators are attractive for low-power frequency conversion via Bragg-scattering four-wave-mixing due to their comb-like resonance spectrum, which allows resonant enhancement of all four waves while maintaining energy and momentum conservation. However, the symmetry of such mode structures limits the conversion efficiency to 50% due to the equal probability of up- and down-conversion. Here, we demonstrate how two coupled microrings enable highly directional conversion between the spectral modes of one of the rings. An extinction between up- and down-conversion of more than 40 dB is experimentally observed. Based on this method, we propose a design for on-chip multiplexed single-photon sources that probabilistically generate photon pairs across many frequency modes of a ring resonator and subsequently convert them to a single frequency—thereby enabling quasi-deterministic photon emission. Our numerical analysis shows that once a photon is generated, it can be converted and emitted into a wave packet having a 90% overlap with a Gaussian with 99% efficiency for a ratio between intrinsic and coupling quality factors of 400.

## 1. Introduction

Four-wave-mixing (FWM) processes have been widely studied in photonic integrated circuits (PICs) because the intensity enhancement in sub-wavelength confinement waveguides significantly reduces the required pump power [1]. Frequency conversion, where a signal field at  $\omega_s$  is converted to an idler field at  $\omega_i$ , is possible via FWM using two strong pump fields at  $\omega_{p_1}$  and  $\omega_{p_2}$  with  $\omega_{p_2} - \omega_{p_1} = \omega_i - \omega_s$ . In this so-called Bragg-scattering FWM (BS-FWM) process [2], photons are annihilated from the fields at  $\omega_s$  and  $\omega_{p_2}$  and created at  $\omega_i$  and  $\omega_{p_1}$ . Frequency conversion is possible with both classical and quantum fields [2, 3] with applications in optical communication [4] as well as quantum information processing [3].

Resonant enhancement of the BS-FWM process is possible using microring resonators if all four frequencies coincide with resonances of the ring. However, if the frequency separation between the pumps is e.g. one free-spectral-range (FSR) of the ring ( $\omega_{p_2} - \omega_{p_1} = \Omega_{\text{FSR}}$ ), then a field at  $\omega_s$  is up-converted to  $\omega_{i+} = \omega_s + \Omega_{\text{FSR}}$  or down-converted to  $\omega_{i-} = \omega_s - \Omega_{\text{FSR}}$  with equal probability. The reason is that the two processes only differ in changing the roles of the pumps as receiver or donor of photons. This limits the conversion efficiency to 50% [5] as illustrated in figures 1(a), (c).

In this work, we demonstrate a PIC device that uses mode-coupling to allow frequency conversion between resonances of a microring resonator with an extinction ratio above 40 dB. The concept (illustrated in figure 1(b)) is based on coupling two rings where the FSR of one is an integer multiple of the other. When their resonances align, the coupling-induced mode-splitting effectively eliminates either the up- or down-converted resonance leading to near-unity conversion efficiency (see figures 1(b), (c)). Another interpretation of the mode-splitting is that the auxiliary ring introduces an additional phase to the field circulating in ring 1 (see appendix A for details). The auxiliary ring may therefore be viewed as a tool for dispersion engineering of ring 1 and this approach has been applied to FWM applications in ring resonators [6, 7]. Dispersion engineering was also used to achieve



unidirectional frequency conversion in fibers by having only the up- or down-conversion process be phase-matched [8, 9].

Our primary motivation for studying frequency conversion in PIC resonator structures is its potential for realizing frequency-multiplexed single photon sources. Quasi-deterministic single photon generation using probabilistic parametric processes, such as spontaneous parametric down-conversion or spontaneous FWM (SFWM), requires multiplexing [10]. This process relies on producing photons probabilistically between several modes representing spatial, temporal, or spectral degrees of freedom of the photons. One of the challenges in multiplexing is to convert photons from any mode into a single output mode without reducing the fidelity of the quantum state. Most multiplexing demonstrations have relied on spatial or temporal modes [11–14], but quantum frequency conversion was recently demonstrated as a powerful tool to enable multiplexing of photons in different spectral modes [9, 15]. The main advantage of using the spectral degree of freedom of photons is that no lossy switches are needed to combine modes after frequency conversion. This is generally not the case for spatial- or temporal degrees of freedom [11–14] where the number of switches (and therefore the total loss) increases with the number of multiplexed modes. For frequency-multiplexing, the number of usable modes is limited by the bandwidth over which efficient frequency conversion is possible. So far, all experimental demonstrations of multiplexing were implemented using fiber or free-space optics due to the difficulty of achieving on-chip quantum feedback control. However, compact and energy efficient sources suitable for large-scale quantum information processing require devices based on PICs. Ring resonators are natural candidates owing to their comb-like mode spectrum (see figure 1(a)), which has been used to demonstrate frequency conversion [5] and high-dimensional entanglement [16].

Based on our demonstration of unidirectional frequency conversion, we propose a PIC single-photon source that multiplexes the dense spectral modes of microring resonators to enable quasi-deterministic emission. Its multiplexing protocol only involves switching the classical pump fields, which significantly reduces the single-photon loss [9]. The device is very compact since photon creation and frequency conversion occur in the same resonator structure. The output photons have very high spectral purity [17], which is essential for high-visibility multi-photon interference. Additionally, we show how the temporal wave packet of emitted photons may be controlled by shaping the BS-FWM pump fields.

This article is organized as follows: in section 2 we present our experimental results demonstrating unidirectional frequency conversion between modes of a ring resonator. Section 3 presents our proposal for using this concept in a PIC implementation of a frequency-multiplexed single-photon source. We conclude in section 4 with a discussion of the challenges involved with realizing our proposal.

## 2. Experimental demonstration of unidirectional frequency conversion

Efficient BS-FWM in ring resonators requires both energy- and momentum conversion, which is achieved when  $n_g(\omega_{p_2}) - n_g(\omega_{p_1}) = n_g(\omega_i) - n_g(\omega_s)$ , with  $n_g$  being the group index of the ring. For our experimental demonstration of unidirectional frequency conversion we used four resonances in relatively close proximity such that the group index was approximately constant over the frequency range of interest. We fabricated a device (shown in figure 2(a)) consisting of two coupled microring resonators realized in a silicon-on-insulator

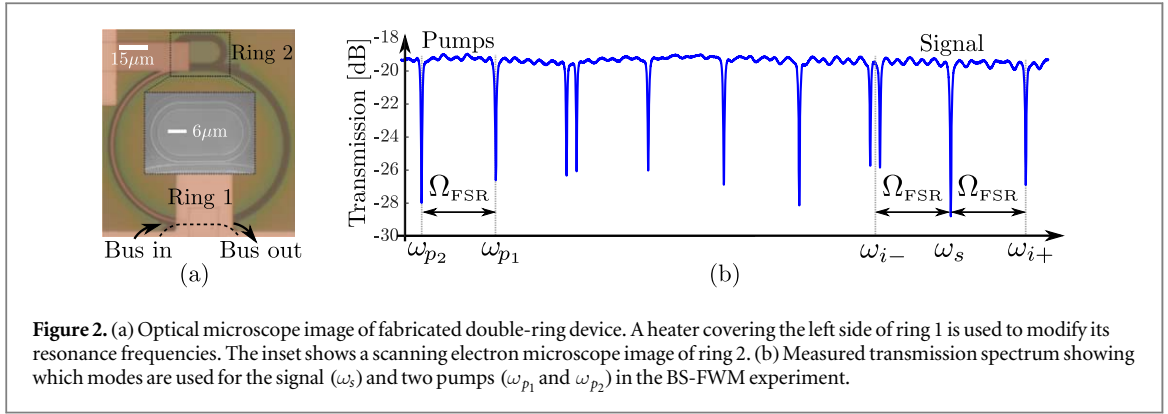


**Figure 2.** (a) Optical microscope image of fabricated double-ring device. A heater covering the left side of ring 1 is used to modify its resonance frequencies. The inset shows a scanning electron microscope image of ring 2. (b) Measured transmission spectrum showing which modes are used for the signal ( $\omega_s$ ) and two pumps ( $\omega_{p_1}$  and  $\omega_{p_2}$ ) in the BS-FWM experiment.

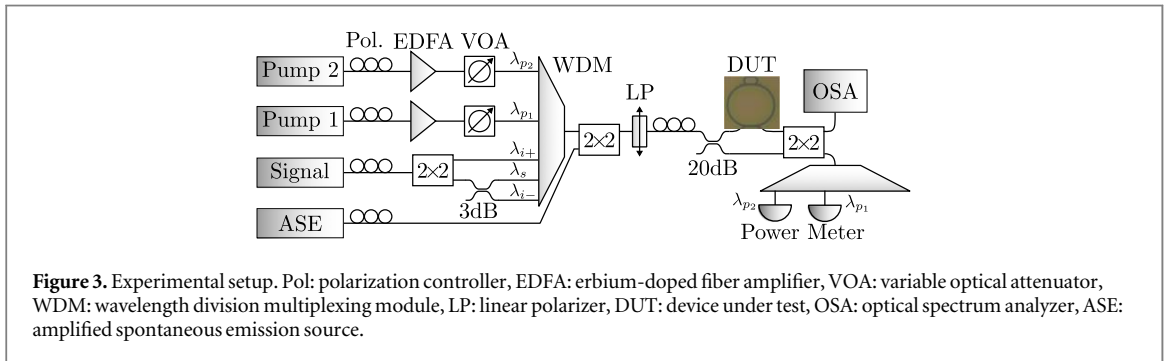


**Figure 3.** Experimental setup. Pol: polarization controller, EDFA: erbium-doped fiber amplifier, VOA: variable optical attenuator, WDM: wavelength division multiplexing module, LP: linear polarizer, DUT: device under test, OSA: optical spectrum analyzer, ASE: amplified spontaneous emission source.

(SOI) material (250 nm silicon on a 3  $\mu\text{m}$  thick buried oxide layer) using electron-beam lithography. The waveguides are 500 nm wide and the circumference of ring 1 (2) is 324  $\mu\text{m}$  (81  $\mu\text{m}$ ) such that the FSR of ring 1,  $\Omega_{\text{FSR}} = 2\pi c/1.55 \text{ nm}$ , is four times smaller than that of ring 2. The device is covered by a 1  $\mu\text{m}$  thick oxide layer on top of which a heating element is formed by a thin titanium wire, see figure 2(a). Grating couplers [18] are used for coupling in and out of the chip.

In the BS-FWM experiment we pump ring 1 on the two resonances at  $\omega_{p_1} = 2\pi c/1553.9 \text{ nm}$  and  $\omega_{p_2} = 2\pi c/1552.3 \text{ nm}$  (see figure 2(b)) using continuous wave (CW) lasers. A weak CW laser is used for the signal and its wavelength is scanned across the resonance at  $\omega_s = 2\pi c/1542.9 \text{ nm}$ . For each wavelength,  $\lambda$ , of the signal laser, the spectrum of the generated idler fields are measured in the vicinity of the up- and down-converted modes at  $\omega_{i+} = 2\pi c/1541.3 \text{ nm}$  and  $\omega_{i-} = 2\pi c/1544.4 \text{ nm}$ , respectively. This gives rise to two-dimensional idler power maps, see figure A4 for an example. Our setup for the BS-FWM experiment is shown in figure 3. The three CW lasers (pump 1, pump 2, and signal) are combined using a WDM module and both input and output can be sent to an OSA using a two-by-two switch. Additionally, the pump output power can be monitored by power meters while tuning their wavelengths to thermally lock them to the ring resonances [5]. A broadband ASE source is used to measure linear transmission spectra.

The heater on ring 1 is used to align the resonances of the two rings. Figure 4(a) shows the measured transmission as a function of wavelength (close to  $\lambda_{i-}$ ) and heater voltage. The spectrum exhibits an avoided crossing typical of strongly coupled systems [19]. From the two-dimensional idler power maps, the diagonal cross-sections (see figure A4) corresponding to the power emitted near the up-converted mode,  $P_{i+}(\lambda, \lambda - \lambda_{\text{FSR}})$ , and down-converted mode,  $P_{i-}(\lambda, \lambda + \lambda_{\text{FSR}})$ , are plotted in figures 4(b)–(d). The corresponding heater voltages are indicated in figure 4(a). The three plots correspond to the resonance of ring 1 being red-detuned (b), aligned (c), and blue-detuned (d) with respect to the resonance of ring 2. Note that the symmetric case in figure 4(c) requires a lower heater voltage compared to figure 2(b) due to the thermal red-shift induced by the pumps. Figures 4(b)–(d) also show transmission spectra of the down-converted mode,  $T_{i-}(\lambda + \lambda_{\text{FSR}})$ , signal mode,  $T_s(\lambda)$ , and up-converted mode,  $T_{i+}(\lambda - \lambda_{\text{FSR}})$ , while the pumps are on. In appendix A.1, we derive expressions for the transmission and conversion efficiency, which are plotted as solid lines in figures 4(b)–(d). The values of model parameters in appendix A.1 were estimated using a step-wise fitting procedure described in appendix B and are listed in table 1. The agreement between theory and measurement in figures 4(b)–(d) suggests that our device is well-described by the model used in appendix A.1. The results from three different heater settings in figure 4 illustrate that maximum directionality of the frequency conversion process is achieved when the resonances of the two rings are exactly aligned (figure 4(c)).

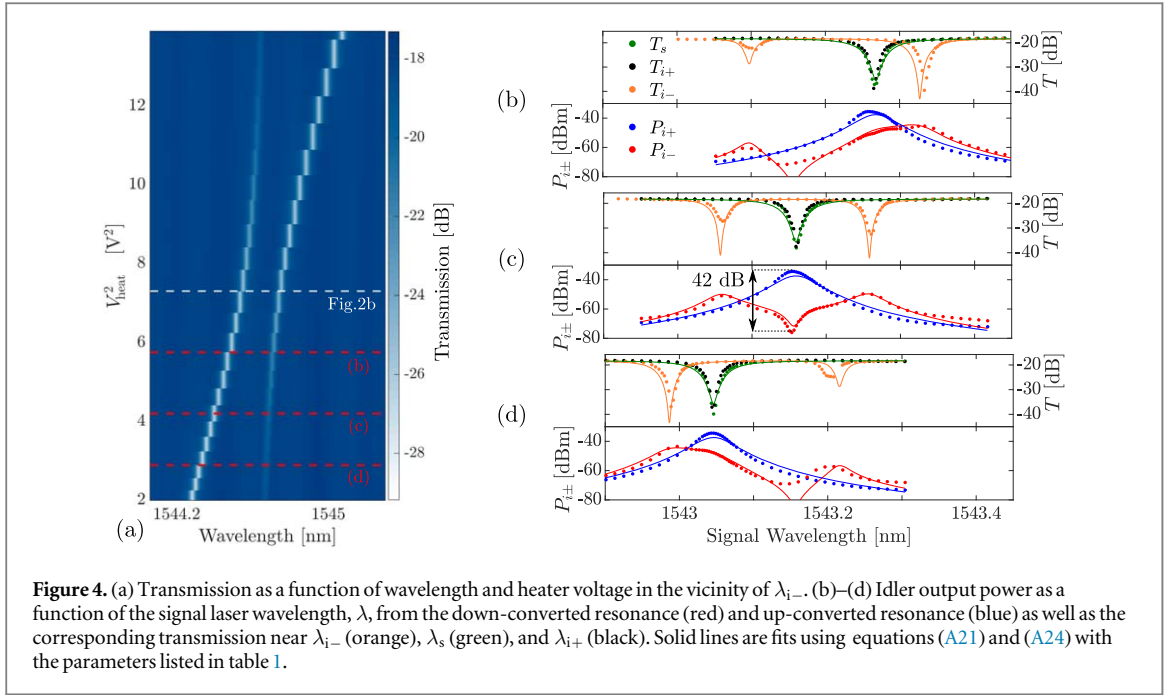


**Table 1.** Device parameters. The in- and out-coupling,  $T_{\text{cpl}}$ , was estimated by assuming the transmission away from any resonance is  $T_{\text{cpl}}^2$ . The power in the bus waveguide immediately before the ring was estimated as  $P_i = T_{\text{cpl}} P_{\text{in},i}$ , where  $P_{\text{in},i}$  is the power measured before the fiber array. The up-conversion efficiency,  $\eta_{i+}$ , was estimated from the ratio of the peak of the up-converted power,  $P_{i+}$ , to the input power,  $P_s$ . The remaining parameters are: the extinction ratio,  $|\zeta|^2$  (defined in equation (A4)), the coupling quality factor,  $Q = \omega_s/\gamma$  (with  $\gamma$  being the coupling rate), the intrinsic quality factor of ring 1 and 2,  $Q_{L_n} = \omega_s/\gamma_{L_n}$  (with  $\gamma_{L_n}$  being the intrinsic loss rates), the ring-ring coupling,  $g$ , the free-carrier absorption loss rate caused by the pumps,  $\gamma_{\text{FCA}}$ , and the BS-FWM inter-modal coupling strength,  $\bar{\chi}$ .

Measured	Fitted
$T_{\text{cpl}} = -9.4$ dB	$Q = 4.4 \times 10^4$
$P_{p1} = 3.9$ dBm	$Q_{L1} = 1.11 \times 10^5$
$P_{p2} = 4.2$ dBm	$Q_{L2} = 1.52 \times 10^5$
$P_s = -11.6$ dBm	$g = 2.86\gamma$
$\eta_{i+} = -22.6$ dB	$\gamma_{\text{FCA}} = 0.36\gamma$
$ \zeta ^2 = 41.7$ dB	$\bar{\chi} = 0.06\gamma$

As the detuning between the resonances is increased (figures 4(b), (d)) the symmetry between up- and down-conversion is increasingly restored.

Our measured conversion efficiency is 0.55% (−22.6 dB) and limited by pump power and two-photon absorption (TPA). Reaching near-unity efficiency requires a material without TPA [5]. The BS-FWM inter-modal coupling strength,  $\bar{\chi}$  may be estimated in two different ways, see equations (A24) and (A27). The resulting values are  $\bar{\chi} = 0.04\gamma$  and  $\bar{\chi} = 0.06\gamma$ , respectively, which also suggests a reasonable consistency within the model.

Our main experimental result is a very high extinction between up- and down-conversion of more than 40 dB when the ring resonances are aligned (see figure 4(c)). We note that the extinction,  $|\zeta(\Omega)|^2$ , is frequency dependent and would therefore be lower for pulsed input fields.

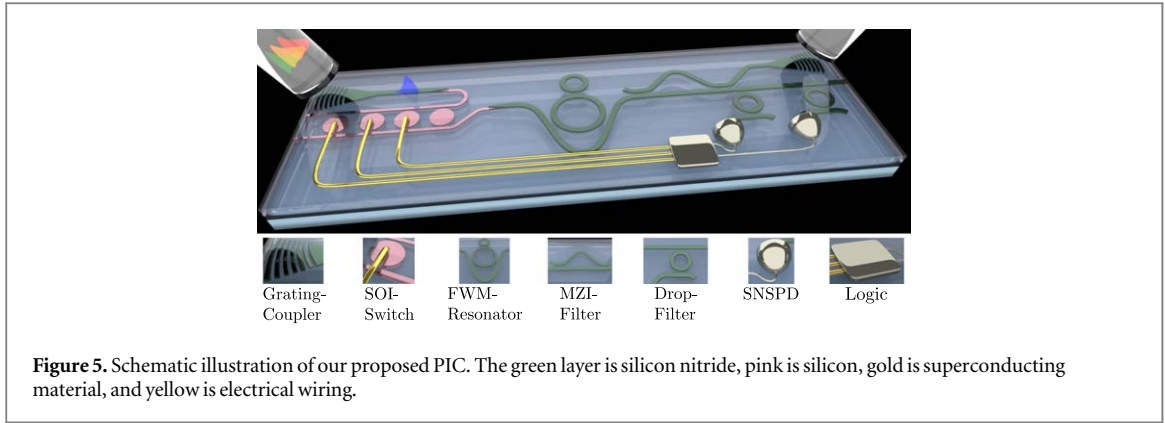


**Figure 5.** Schematic illustration of our proposed PIC. The green layer is silicon nitride, pink is silicon, gold is superconducting material, and yellow is electrical wiring.

### 3. On-chip frequency-multiplexing device

Having demonstrated a device concept enabling near-unity frequency conversion efficiency between ring resonator modes allows us to design spectrally multiplexed single-photon sources for implementation in PICs. In order to both generate and frequency convert photons in the same resonator, control over the cavity-waveguide coupling for different modes is required. Interferometric coupling [20] may be used to generate photon pairs where one, the signal photon, is decoupled from the bus waveguide whereas the other, the idler photon, is strongly coupled. Then, the signal photon remains in the resonator while the idler is routed to a detector that controls switches allowing specific BS-FWM pumps to convert the signal photon. A major advantage of our proposal is the elimination of spatial switches used in e.g. [21] by converting signal photons to a common output mode,  $\omega_{\text{out}}$ , which is strongly coupled to the bus waveguide. It is even possible to shape the wave packet of the output photons by tailoring the temporal shape of the BS-FWM pumps, which we show in section 3.3.

Our proposed PIC implementation is illustrated in figure 5. It is based on a scalable multilayer silicon nitride (SiN) on SOI platform [22, 23] that enables individual photons to be produced, frequency converted, and routed in the SiN layer with low loss and no TPA while switching of the pump fields occurs in the silicon layer [24, 25]. Photon pair generation by SFWM and frequency conversion by BS-FWM occur in the FWM-resonator. It resembles the device in figure 2(a) except for its interferometric coupling, which is achieved by forming a Mach-Zehnder interferometer (MZI) between the bus waveguide and part of ring 1 [20]. Frequency-selective ring resonator drop-filters [26] connect each idler mode to a specific superconducting-nanowire-single-photon-detector (SNSPD). The electrical signal from the detector is processed [27] and used to flip switches [24, 25] controlling the passage of the BS-FWM pump fields. The rightmost SOI switch in figure 5 controls the passage of the SFWM pump at  $\omega_p$  (blue pulse), its neighbor controls the common BS-FWM pump at  $\omega_{p_2}$  (green pulse), while the rest control BS-FWM pumps at  $\omega_{p_1,n}$  (yellow and red pulses) for each spectral multiplexing mode,  $n \in \mathbb{Z}$ . Note that the illustration in figure 5 is an example using  $N = 2$  spectral modes.

The emission protocol consists of the following two steps: first, a SFWM pump pulse at  $\omega_p$  generates photons at any of the mode pairs  $\omega_{s,n}$  and  $\omega_{i,n}$ , where  $s$  ( $i$ ) means signal (idler) and  $n \in \mathbb{Z}$  enumerates the spectral multiplexing modes. Signal photons remain in the resonator while idler photons are routed to the SNSPDs. Second, an idler detection causes two SOI switches [24, 25] to flip allowing BS-FWM pumps at  $\omega_{p_2}$  and  $\omega_{p_1,n}$  (with  $\omega_{p_2} - \omega_{p_1,n} = \omega_{\text{out}} - \omega_{s,n}$ ) to enter the resonator and frequency convert the signal photon to the common output at  $\omega_{\text{out}}$ . The output mode is strongly coupled to the bus waveguide causing the converted photon to exit the resonator and couple into the output waveguide through the MZI-filter.

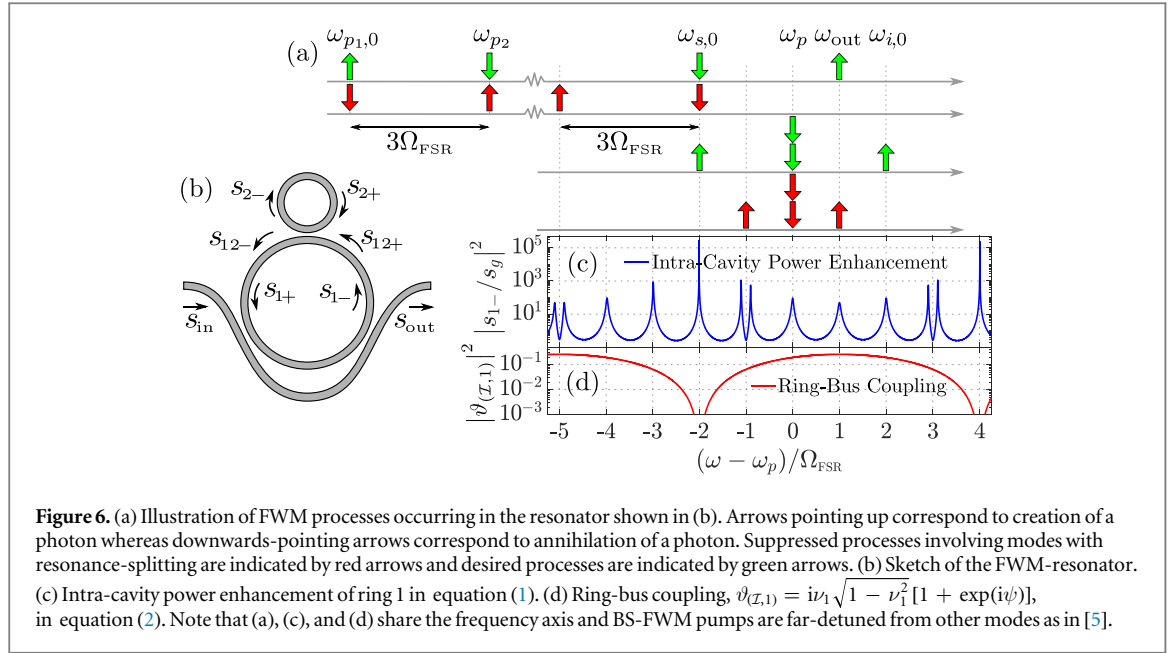
We stress that the switches only operate on the classical pump fields - making their insertion loss far less critical than if they operated on single photons.

#### 3.1. Interferometrically coupled resonator

The FWM-resonator is sketched again in figure 6(b) with the fields,  $s$ , in various parts of the device indicated. Considering a case without input fields ( $s_{\text{in}} = 0$ ) and a field,  $s_g$ , being generated inside ring 1, the intra-cavity power enhancement of ring 1 is defined as (see appendix A.3 for details)

$$\left| \frac{s_1}{s_g} \right|^2 = \left| \frac{1}{1 - \bar{C}_{1,1}^{(Z,1)} e^{i\Phi_1} \bar{h}_{12}} \right|^2, \quad \bar{h}_{12} = \frac{\nu_2 - e^{i\Phi_2}}{1 - \nu_2 e^{i\Phi_2}}, \quad (1)$$

where  $\Phi_1$  ( $\Phi_2$ ) is the round-trip phase of ring 1 (2). The through-coupling coefficient of the coupling region between the rings is  $\nu_2$ . The matrix describing the MZI coupling region is



$$\bar{C}^{(z,1)} = \begin{bmatrix} \nu_1^2 - e^{i\psi}(1 - \nu_1^2) & i\nu_1\sqrt{1 - \nu_1^2}(1 + e^{i\psi}) \\ i\nu_1\sqrt{1 - \nu_1^2}(1 + e^{i\psi}) & \nu_1^2(1 + e^{i\psi}) - 1 \end{bmatrix}, \quad (2)$$

where  $\psi$  is the phase imbalance of the MZI and the directional couplers are assumed identical with a through-coupling coefficient  $\nu_1$ . The blue curve in figure 6(c) plots equation (1) and the red curve plots the off-diagonal elements of the MZI coupling matrix in equation (2) for a FWM-resonator design where the length of ring 1 is four times larger than ring 2 and six times larger than the path-length difference of the coupling-interferometer. Resonances of ring 1 are enumerated relative to the SFWM pump as  $\omega_j = \omega_p + j\Omega_{\text{FSR}}$  with  $j \in \mathbb{Z}$  and ring 2 has resonances at  $\omega_{-1+4n}$  with  $n \in \mathbb{Z}$ . Figure 6(c) shows that signal modes at  $\omega_{s,n} = \omega_{-2+6n}$  are decoupled from the bus waveguide whereas the pump ( $\omega_p$ ), idler ( $\omega_{i,n} = \omega_{2-6n}$ ), and output mode ( $\omega_{\text{out}} = \omega_1$ ) are strongly coupled. Note that  $n$  attains both positive and negative values so that signal modes exist on both sides of  $\omega_p$ . Figure 6(a) illustrates the relevant FWM processes of the pair creation and frequency conversion for  $n = 0$ . Direct generation of photons at  $\omega_{\text{out}}$  ( $2\omega_p \rightarrow \omega_{\text{out}} + \omega_{-1}$ ) must be avoided since emission should only occur after step two of the protocol. The process is indeed suppressed due to mode-splitting at  $\omega_{-1}$ . Additionally, mode-splittings at  $\omega_{-5+12n}$  ensure suppression of the conversion process  $\omega_{s,n} + \omega_{p_1,n} \rightarrow \omega_{-5+12n} + \omega_{p_2}$ , whereas the desired multiplexing conversion in the opposite direction,  $\omega_{s,n} + \omega_{p_2} \rightarrow \omega_{\text{out}} + \omega_{p_1,n}$ , is resonantly enhanced.

In the high conversion efficiency regime, it becomes important to consider cascaded BS-FWM processes in which photons get converted several times before coupling into the bus waveguide. This severely limits the conversion efficiency without interferometric coupling. In appendix C we show that the conversion efficiency is limited to 50% even for perfect unidirectionality by including first-order cascaded FWM. However, we note that signal modes in figure 6(c) are located symmetrically around  $\omega_{\text{out}}$ , such that

$$|\omega_{s,n} - \omega_{\text{out}}| = |\omega_{\text{out}} - \omega_{s,-(n-1)}|, \quad n \in \mathbb{Z}. \quad (3)$$

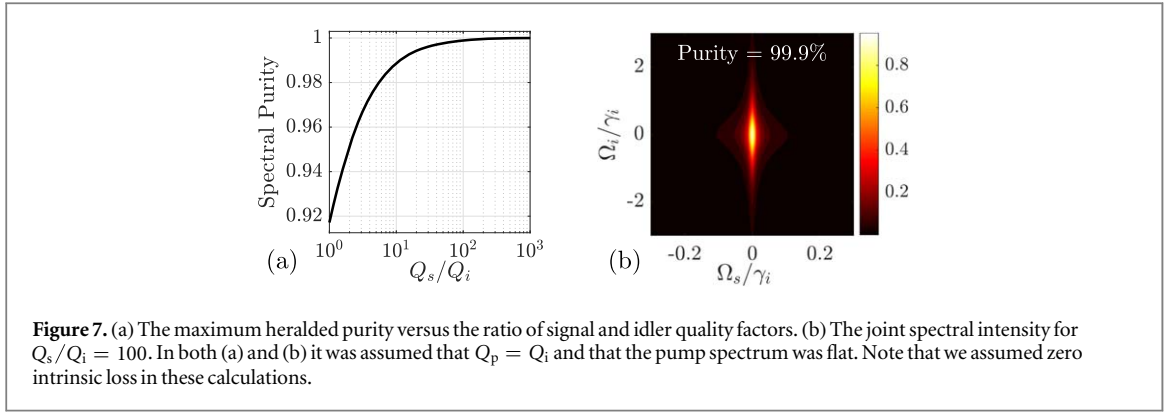
This ensures that the first-order cascaded BS-FWM process is  $\omega_{s,n} \rightarrow \omega_{\text{out}} \rightarrow \omega_{s,-(n-1)}$ , where the photon ends on another signal mode. Any higher-order process is suppressed by mode-splitting and the photon is eventually converted back to  $\omega_{\text{out}}$ .

Undesired SFWM producing photons at  $\omega_{\text{out}}$  or  $\omega_{s,n}$  from the BS-FWM pumps may be suppressed by placing the BS-FWM and SFWM pumps on either side of the zero-dispersion wavelength matching their group indices [5]. In this way, the undesired SFWM processes are not phase-matched and therefore suppressed. If the path-length difference of the MZI-filter in figure 5 is two times shorter than ring 1 it may be adjusted to separate odd- from even-numbered modes such that  $\omega_{\text{out}}$  is dropped to the output waveguide while  $\omega_p$  and all idler modes continue in the bus waveguide towards the SNSPDs.

### 3.2. Spectral correlations of generated photon pairs

An important advantage of our proposed design is its ability to produce photons with very high spectral purity. It has been shown that the spectral purity of photons emitted from a resonator where idler, pump, and signal modes are identical is limited to 92% even for a flat pump spectrum [17, 28]. In [17] it was shown that using interferometric coupling to increase the linewidth of the pump relative to the signal and idler enables arbitrarily





high spectral purity. Another solution is to modify the pump spectrum as shown in [29]. Our design achieves a signal linewidth,  $\gamma_s$ , that is smaller than the pump,  $\gamma_p$ , and idler,  $\gamma_i$ . Figure 7(a) plots the spectral purity of our device as a function of the ratio between the quality factors ( $Q_j = \omega_j/\gamma_j$  with  $j$  labeling the resonance) of the signal and idler modes when assuming  $Q_p = Q_i$  and a flat pump spectrum (see appendix D for details). We note that this is the purity of signal photons being leaked into the environment and leave the purity analysis of photons coupled out after frequency conversion for future work. Figure 7(a) shows that the spectral purity rapidly increases towards unity as  $Q_s/Q_i$  increases. In the next section, we show that the frequency conversion efficiency increases with  $Q_L/Q_i$  (were  $Q_L = \omega_p/\gamma_L$ ), which means that the spectral purity increases simultaneously since  $Q_s \approx Q_L$  for the interferometrically coupled device. For  $Q_s/Q_i = 100$ , the resulting joint spectral intensity is plotted in figure 7(b). It displays a broad idler distribution and narrow signal distribution, with negligible correlations between signal and idler frequencies, giving rise to a spectral purity of 99.9%.

### 3.3. Photon frequency conversion

The second step of the emission protocol consists of frequency converting a signal photon from the signal mode ( $s$ ) to the output mode (denoted  $o$  here for brevity). For a material without TPA, the efficiency is only limited by the ring-ring coupling in the form  $G = g/\sqrt{\gamma_L(\gamma_L + \gamma_o)}$  and the ratio between the coupling- and loss rates,  $Q_L/Q_o$ . Here, we are interested in emitting photons into a specific wave packet described by the function  $S_{\text{out},o}(t)$ . Photons with time-symmetric wave packets are particularly interesting for e.g. two-photon gates [30] and reducing sensitivity to timing jitter in two-photon interference [31] so we consider a Gaussian wave packet as a specific example

$$S_{\text{out},o}^{\text{Gauss}}(t) = \sqrt{\frac{2}{\Delta t}} \left( \frac{\ln(2)}{\pi} \right)^{\frac{1}{4}} \exp\left(-2 \ln(2) \frac{(t - t_0)^2}{\Delta t^2}\right). \quad (4)$$

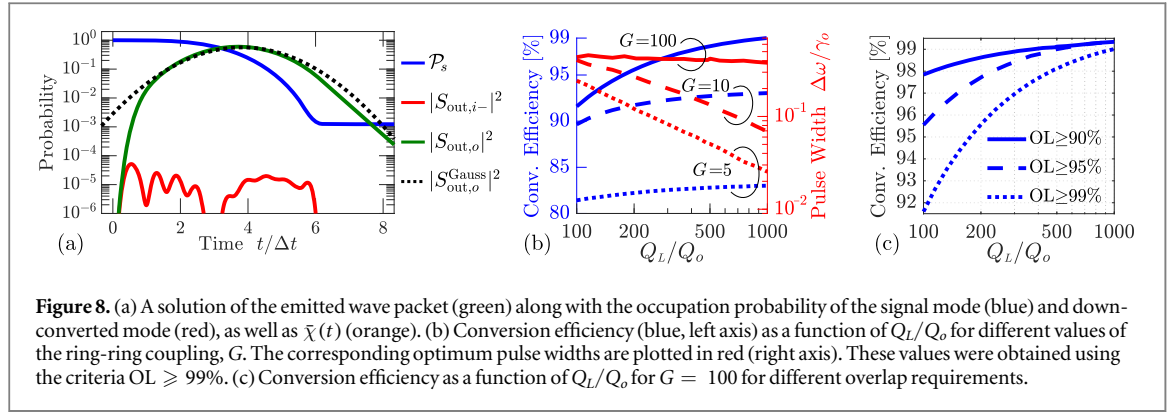
It has a temporal full width at half maximum (FWHM)  $\Delta t$ , spectral width  $\Delta\omega = 4 \ln(2)/\Delta t$ , and its squared amplitude integrates to 1. In appendix E, we derive the temporal shape of  $\bar{\chi}(t)$  required to achieve the desired output wave packet. We use this result when solving the equations of motion in equation (A56) for the cavity field amplitudes of the signal ( $A_s$ ), output ( $A_o$ ), down-converted ( $A_{i-}$ ), and auxiliary ( $B$ ) mode as well as the output wave packet ( $S_{\text{out},o}$ ). The deviation of the output,  $S_{\text{out},o}$ , from the desired wave packet,  $S_{\text{out},o}^{\text{Gauss}}$ , is quantified by the conversion efficiency

$$\eta_{\text{out}} = \int_0^\infty |S_{\text{out},o}(t)|^2 dt, \quad (5)$$

and overlap

$$\text{OL} = \langle S_{\text{out},o} | S_{\text{out},o}^{\text{Gauss}} \rangle = \frac{1}{\eta_{\text{out}}} \left| \int_0^\infty S_{\text{out},o}^*(t) S_{\text{out},o}^{\text{Gauss}}(t) dt \right|^2. \quad (6)$$

Figure 8(a) plots the solution to equation (A56) for a specific case of  $Q_L/Q_o = 500$ ,  $G = 100$ , and  $\Delta\omega/\gamma_o = 0.38$ . The occupation probabilities are defined as  $\mathcal{P}_n \equiv |A_n|^2$  and the absolute square of the output fields correspond to the probability density of observing the photon at different times. Assuming that a photon occupies the signal mode at time  $t = 0$ , the blue curve in figure 8(a) shows how the probability decays as the photon is converted to the output mode and coupled out of the resonator. Comparing the green and dotted black curves illustrates that the output wave packet has a large overlap with a Gaussian with deviations only in the tails. Figure 8(a) further shows that conversion to the  $i$ -mode (red curve) is highly suppressed even for a pulsed output as opposed to the suppression of CW fields in section 2. However, pulsed operation requires a larger value of  $G$  than CW operation to achieve a large suppression.



To investigate the influence of loss and out-coupling through the down-converted mode, we evaluate the figures of merit for different values of  $Q_L/Q_o$  and  $G$ . The results are shown in figures 8(b), (c). In figure 8(b) we require an overlap of at least 99%, and it is seen that 99% conversion efficiency is achievable with  $G = 100$  and  $Q_L/Q_o \sim 1000$ . As  $G$  decreases, the bandwidth of large extinction between up- and down-conversion also decreases. This necessitates narrow bandwidth pulses, which are longer in time leading to higher loss during emission. Therefore, both the conversion efficiency and optimum pulse bandwidth decreases with decreasing  $G$  as illustrated in figure 8(b).

If the overlap requirement is relaxed, the conversion efficiency can be significantly increased as illustrated in figure 8(c). This demonstrates that there exists a trade-off between conversion efficiency and the desired temporal wave packets of the emitted photons, which is important to keep in mind for different applications of the source.

#### 4. Discussion

With our experimental demonstration we have shown how to overcome limitations in the efficiency of frequency conversion between modes of PIC ring resonators due to their symmetric mode spectrum. Achieving on-chip multiplexing requires a latency of the quantum feedback below the photon storage time, which is only possible by placing switches in close proximity to the SNSPDs. The SOI-based switches must then be functional at cryogenic temperatures, which has recently been demonstrated [24]. Driving the switches using the weak electrical signals output from the SNSPDs is challenging, but devices capable of amplification and logic operations have been developed [27]. Single chip filtering with sufficient extinction for pump rejection has recently been demonstrated [26]. However, the BS-FWM pumps must be even higher power than the SFWM pump and further progress in on-chip filtering is necessary. Additionally, it is necessary to statically tune the rings of the FWM-resonator as well as the drop filters. Opto-electro-mechanical tuning of the refractive index in waveguides is suitable for cryogenic operation and demonstrations of large index shifts with low loss have been presented [32]. The number of available spectral multiplexing modes depends on the bandwidth over which  $|\omega_{p_2} - \omega_{p_1, n}| \approx |\omega_{out} - \omega_{s, n}|$ , relative to the FSR of ring 1.  $N = 16$  is the lower limit to achieve 99% fidelity of the single-photon state assuming zero loss and number-resolving detectors [33]. Since frequency-combs with hundreds of modes have been realized in SiN microrings [34] it seems reasonable to expect that several tens of multiplexing modes would be possible (note that only every sixth mode is available for multiplexing with our scheme in figure 6).

In conclusion, we have experimentally demonstrated that unidirectional frequency conversion between modes of ring resonators is possible with more than 40 dB extinction. Our theoretical investigation shows that this leads to near-unity conversion efficiency and based on this, we proposed a scheme for PIC frequency-multiplexed single photon sources with high performance. For instance, figures 7(b) and 8(c) show that 99% conversion efficiency and spectral purity is possible for  $Q_L/Q_i \sim 400$ . If, for instance, the pump, idler, and output modes have coupling  $Q$ s of  $10^4$  the corresponding intrinsic  $Q$  must be  $4 \times 10^6$ , which is well below what has been demonstrated [35]. Electronic feedback control at these short timescales remains to be demonstrated, but since many quantum information processing tasks rely on it, we are optimistic that the field will progress sufficiently. For an analysis of the full system efficiency including latency in the quantum feedback as well as detector efficiency, we refer to [21]. Importantly, we note that extraction of the created signal photon from the ring is included in the frequency conversion efficiency here, whereas the loss associated with this process was not treated in [21]. We consider our proposal to be a very promising route to on-chip multiplexed single-photon sources for near-term implementation. The constituent components have been demonstrated individually

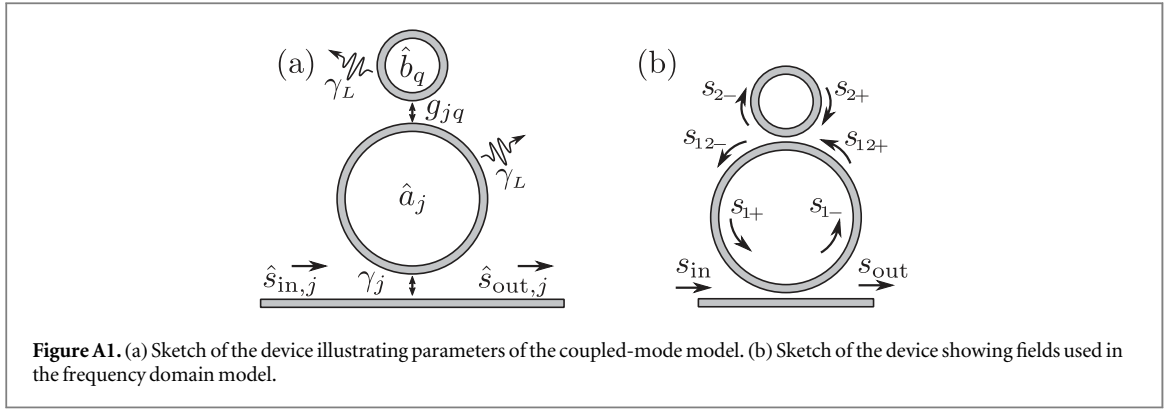


**Figure A1.** (a) Sketch of the device illustrating parameters of the coupled-mode model. (b) Sketch of the device showing fields used in the frequency domain model.

[23, 24, 26, 27, 32] and switching only the classical fields significantly improves the loss-budget over other types of multiplexing.

## Acknowledgments

This work was supported by the Danish National Research Foundation through the Center of Excellence SPOC (Silicon Photonics for Optical Communication), DNRFF 123. M H acknowledges funding from VILLUM FONDEN.

## Appendix A. Device models

It is useful to consider two descriptions of the coupled resonators in this work. One, which we denote the coupled-mode model (CMM), is convenient for modeling the dynamics of the system and predict its performance. The other, denoted the frequency domain model (FDM), is useful for device design. Figure A1(a) shows a sketch of the device indicating parameters in the CMM and figure A1(b) shows the fields used in the FDM analysis. Below, we go through each model description and explain how to relate their parameters. This ensures that geometrical properties of devices can be related to their performance and thereby assist the design process.

### A.1. Coupled-mode model

The CMM is the standard description used in open quantum systems where the cavity resonances are treated as discrete modes that couple to each other and the continuous waveguide-modes with coupling rates  $g_{jq}$  and  $\gamma_j$ , respectively. The system is modeled by the Hamiltonian  $H = H_L + H_{NL}$  with [36]

$$H_L = \sum_j \omega_j \hat{a}_j^\dagger \hat{a}_j + \sum_j i \sqrt{\frac{\gamma_j}{2\pi}} \int_{-\infty}^{\infty} d\omega [\hat{a}_j \hat{s}^\dagger(\omega) - \hat{a}_j^\dagger \hat{s}(\omega)] + \int_{-\infty}^{\infty} d\omega \omega \hat{s}^\dagger(\omega) \hat{s}(\omega) + \omega_b \hat{b}^\dagger \hat{b} + g(\hat{a}_i^\dagger \hat{b} + \hat{b}^\dagger \hat{a}_{i-}), \quad (\text{A1})$$

where  $j \in \{s, i-, i+\}$ . The nonlinear part is

$$H_{NL} = \chi(\hat{a}_1^\dagger \hat{a}_{i+}^\dagger \hat{a}_2 \hat{a}_s + \hat{a}_2^\dagger \hat{a}_{i-}^\dagger \hat{a}_1 \hat{a}_s) + \text{h.c.} \quad (\text{A2})$$

The heat bath responsible for the loss rate,  $\gamma_L$ , is not explicitly included in  $H_L$  but the loss rates are included in operator equations of motion (see [37] for the necessary derivations). As illustrated in figure A1(a), the modes in rings 1, 2, and the bus waveguide are represented by the annihilation operators  $\hat{a}_j$ ,  $\hat{b}_q$ , and  $\hat{s}_j$ , respectively. We only consider one mode of ring 2, which only couples to mode  $i$ —of ring 1, so we have dropped the subscripts on  $\hat{b}$  and  $g$  in equation (A1).

Equations of motion for the electric fields of the cavity modes may be found using the Hamiltonian in equations (A1) and (A2) [38]

$$\dot{A}_s = -\frac{\Gamma_s}{2} A_s - i\bar{\chi}^* A_{i+} - i\bar{\chi} A_{i-} - \sqrt{\gamma_s} S_{\text{in},s} \quad (\text{A3a})$$

$$\dot{A}_{i+} = -\frac{\Gamma_{i+}}{2}A_{i+} - i\bar{\chi}A_s - \sqrt{\gamma_{i+}}S_{in,i+} \quad (\text{A3b})$$

$$\dot{A}_{i-} = -\frac{\Gamma_{i-}}{2}A_{i-} - i\bar{\chi}^*A_s - igB - \sqrt{\gamma_{i-}}S_{in,i-} \quad (\text{A3c})$$

$$\dot{B} = \left(-i\delta_{ab} - \frac{\gamma_L}{2}\right)B - igA_{i-} \quad (\text{A3d})$$

$$S_{out,j} = S_{in,j} + \sqrt{\gamma_j}A_j, \quad j \in \{s, i-, i+\}. \quad (\text{A3e})$$

The fields in equation (A3) are slowly varying amplitudes defined with reference to the mode resonances  $a_j(t) = A_j(t)\exp(-i\omega_j t)$  and  $s_{in,j/out,j}(t) = S_{in,j/out,j}(t)\exp(-i\omega_j t)$ . The field in ring 2 is  $b(t) = B(t)\exp(-i\omega_{i-}t)$ , which gives rise to the detuning  $\delta_{ab} = \omega_b - \omega_{i-}$  in equation (A3d). The time-dependent nonlinearity due to the BS-FWM pumps is  $\bar{\chi}^* = \chi \langle \hat{a}_{p_1} \hat{a}_{p_2}^\dagger \rangle$  and  $\Gamma_j = \gamma_j + \gamma_L$  with  $j \in \{s, i-, i+\}$ . In the linear regime,  $\bar{\chi} = 0$ , equations (A3c) and (A3d) decouple from the rest and describe two coupled resonators. In the strong coupling regime,  $g > \gamma_{i-}/4$ , linear superpositions of  $A_{i-}$  and  $B$  form uncoupled super-modes with modified resonance frequencies. If  $\omega_{i-} = \omega_b$ , the eigenfrequencies of the super-modes are shifted by  $\pm\sqrt{g^2 - (\gamma_{i-}/4)^2}$  relative to the degenerate resonances of  $A_{i-}$  and  $B$ . This mode-splitting is observed in figure 2(b) for every fourth mode of ring 1 because the resonances of each ring are aligned and the FSR of ring 2 is four times larger than that of ring 1.

To analyze the frequency conversion properties of the device, we make the simplifying assumptions  $\gamma_{i+} = \gamma_{i-} = \gamma_i$  and  $\bar{\chi} = \bar{\chi}^*$ . For CW pump fields, equation (A3) may be solved using Fourier transforms. From the solution, we define the extinction ratio

$$\zeta(\Omega) = \frac{\tilde{S}_{out,i+}(\Omega)}{\tilde{S}_{out,i-}(\Omega)} = \frac{4g^2}{[\gamma_L + i2(\delta_{ab} - \Omega)](\Gamma_i - i2\Omega)} + 1, \quad (\text{A4})$$

where  $\Omega$  is the frequency separation of each mode from its resonance,  $\tilde{A}_j(\Omega) = \tilde{a}_j(\Omega + \omega_j)$ , as well as the separation of the input field from the signal resonance,  $\tilde{S}_{in,s}(\Omega) = \tilde{s}_{in,s}(\Omega + \omega_s)$ . The  $\sim$  is used to indicate frequency domain fields. The maximum extinction is found for  $\Omega = 0$  and  $\delta_{ab} = 0$

$$\zeta^{\max} = \frac{4g^2}{\gamma_L \Gamma_i} + 1 = 4G^2 + 1, \quad (\text{A5})$$

where the normalized coupling parameter  $G \equiv g/\sqrt{\gamma_L \Gamma_i}$  was defined. The up-conversion efficiency,

$$\eta_{i+} = \left| \frac{\tilde{S}_{out,i+}}{\tilde{S}_{in,s}} \right|^2 = \left| \frac{4\sqrt{\gamma_i \gamma_s} \bar{\chi}}{(\Gamma_i - i2\Omega)(\Gamma_s - i2\Omega) + 4\bar{\chi}^2(1 + \zeta^{-1})} \right|^2, \quad (\text{A6})$$

has a maximum of

$$\eta_{i+}^{\max} = \frac{1 + 4G^2}{2 + 4G^2} \frac{\gamma_i \gamma_s}{\Gamma_i \Gamma_s}, \quad (\text{A7})$$

which is achieved when  $\delta_{ab} = \Omega = 0$  and for a nonlinearity

$$\bar{\chi}^{\max} = \frac{1}{2} \sqrt{\frac{1 + 4G^2}{2 + 4G^2}} \sqrt{\Gamma_i \Gamma_s}. \quad (\text{A8})$$

Equations (A6) and (A7) are identical to equations (28) and (32) in [38] in the limit  $G \rightarrow \infty$  (note the factor of 2 difference in our definition of decay rates). In the limit of large  $G$  and highly over-coupled ring modes, equation (A7) may be written as

$$\eta_{i+}^{\max} \approx \left(1 - \frac{1}{4G^2}\right) \left(1 - \frac{Q_s + Q_i}{Q_L}\right), \quad (\text{A9})$$

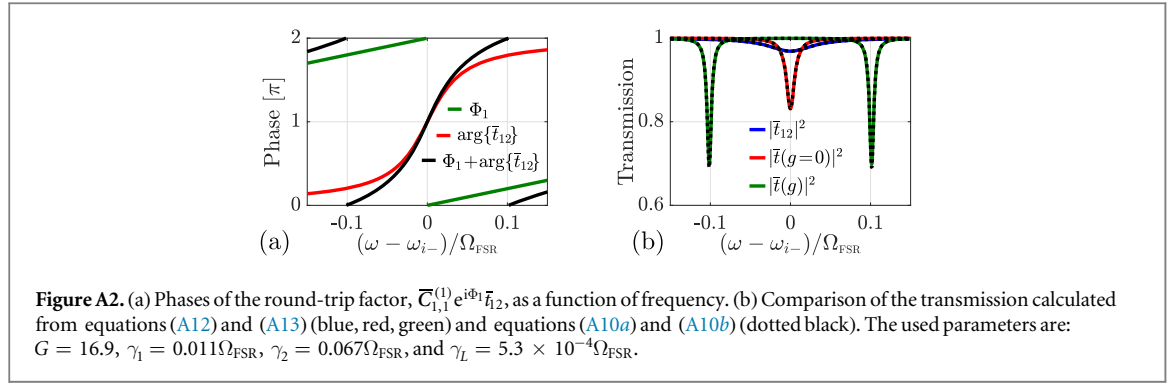
which clearly shows the scaling with  $G$  and the ratio of coupling- to intrinsic quality factor ( $Q_j = \omega_j/\gamma_j$ ).

Reaching 99% conversion efficiency requires  $G \sim 10$  and  $Q_L/Q_j \sim 100$  with  $j \in \{s, i\}$ . The linear transmission in the vicinity of  $\omega_{i-}$  and  $\omega_{i+}$  is

$$t_{i-}(\Omega) = \frac{S_{out,i-}(\Omega)}{S_{in,i-}(\Omega)} = 1 - \frac{\gamma_{i-}}{\frac{\Gamma_{i-}}{2} - i\Omega + \frac{g^2}{\gamma_L/2 - i(\Omega - \delta_{ab})}} \quad (\text{A10a})$$

$$t_{i+}(\Omega) = \frac{S_{out,i+}(\Omega)}{S_{in,i+}(\Omega)} = 1 - \frac{\gamma_{i+}}{\frac{\Gamma_{i+}}{2} - i\Omega}, \quad (\text{A10b})$$

where  $\Omega$  again is the frequency separation from  $\omega_{i-}$  in equation (A10a) and from  $\omega_{i+}$  in equation (A10b). The transmission spectra in equation (A10) are found by assuming all input fields in equation (A3) are zero except  $S_{in,i-}$  for equation (A10a) and  $S_{in,i+}$  for equation (A10b).



## A.2. Frequency domain model

In the FDM, the fields everywhere in the device (see figure A1 (b)) are connected by transfer matrices. We assume the directional couplers are well-described by a matrix,  $C^{(n)}$ , such that

$$\begin{bmatrix} s_{1-} \\ s_{\text{out}} \end{bmatrix} = C^{(1)} \begin{bmatrix} s_{1+} \\ s_{\text{in}} \end{bmatrix}, \quad \begin{bmatrix} s_{2-} \\ s_{12-} \end{bmatrix} = C^{(2)} \begin{bmatrix} s_{2+} \\ s_{12+} \end{bmatrix} \quad (\text{A11a})$$

$$s_{12+} = s_{1-} e^{i\frac{\phi_1}{2}}, \quad s_{1+} = s_{12-} e^{i\frac{\phi_1}{2}}, \quad s_{2+} = s_{2-} e^{i\phi_2}. \quad (\text{A11b})$$

Solving equation (A11) we find the transmission,  $t_{12}$ , of the intra-cavity field in ring 1 when passing ring 2 and the transmission,  $t$ , through the bus waveguide

$$t_{12} = \frac{s_{12-}}{s_{12+}} = C_{2,2}^{(2)} + \frac{C_{1,2}^{(2)} C_{2,1}^{(2)} e^{i\phi_2}}{1 - C_{1,1}^{(2)} e^{i\phi_2}} \quad (\text{A12})$$

$$t = \frac{s_{\text{out}}}{s_{\text{in}}} = C_{2,2}^{(1)} + \frac{C_{1,2}^{(1)} C_{2,1}^{(1)} e^{i\phi_1} t_{12}}{1 - C_{1,1}^{(1)} e^{i\phi_1} t_{12}}. \quad (\text{A13})$$

The coupling regions are assumed to be described by symmetric transfer matrices

$$C^{(n)} = e^{i\theta_n} \begin{bmatrix} \nu_n & i\sqrt{1 - \nu_n^2} \\ i\sqrt{1 - \nu_n^2} & \nu_n \end{bmatrix}, \quad (\text{A14})$$

where  $\theta_n$  is the phase accumulated along the directional coupler and  $\nu_n$  is the through-coupling coefficient. The phase accumulated through a length  $L$  is  $k(\omega)L$  with the propagation constant approximated by

$$k(\omega) \approx k(\omega_{\text{ref}}) + \frac{\partial k}{\partial \omega} \Delta\omega = \frac{\tilde{n}_{\text{eff}} \omega_{\text{ref}}}{c} + \frac{n_g}{c} \Delta\omega, \quad (\text{A15})$$

where  $\Delta\omega = \omega - \omega_{\text{ref}}$ . The imaginary part of the complex refractive index,  $\tilde{n}_{\text{eff}} = n'_{\text{eff}} + in''_{\text{eff}}$ , is related to the linear amplitude loss coefficient and intensity loss rate by

$$\alpha_L = \frac{\omega_{\text{ref}} n''_{\text{eff}}}{c} = \frac{\gamma_L n_g}{2c}. \quad (\text{A16})$$

The round-trip loss of the circulating field in ring 1 due to coupling to the bus waveguide is  $|C_{1,1}^{(1)}| = \nu_1$  and a connection to the CMM is given by

$$\exp[-\gamma_1 \tau_{\text{RT},1}] = \nu_1^2 \Rightarrow \gamma_1 = -\frac{c}{n_g L_1} \ln(\nu_1^2), \quad (\text{A17})$$

where  $\tau_{\text{RT},1}$  is the round-trip time of ring 1. The coupling rate between the rings,  $g$ , can be related to the parameters of the FDM by considering the modification that ring 2 imposes on the circulating field in ring 1. Every time the field passes by ring 2 it acquires the amplitude and phase contained in  $t_{12}$  of equation (A12). This is seen from the round-trip term,  $C_{1,1}^{(1)} e^{i\phi_1} t_{12}$ , in the denominator on the right hand side of equation (A13). Defining  $\bar{C}^{(n)} = C^{(n)} e^{-i\theta_n}$ , and  $\bar{t}_{12} = t_{12} e^{-i\theta_2}$ , the round-trip term is  $\bar{C}_{1,1}^{(1)} e^{i\Phi_1} \bar{t}_{12}$ , where  $\Phi_1 = \phi_1 + \theta_1 + \theta_2$  is the round-trip phase of ring 1 without coupling between the rings. In this form, it is clear that the phase of  $\bar{t}_{12}$  modifies the resonance condition of ring 1. Figure A2(a) plots the phases of the round-trip term when both rings have a resonance at  $\omega_{i-}$ . Since  $\arg\{\bar{t}_{12}(\omega_{i-})\} = \pi$ , the coupled system is anti-resonant at  $\omega_{i-}$  and the black curve shows that two new resonances appear at  $\omega_{i-} \pm 0.1\Omega_{\text{FSR}}$  where the total round-trip phase equals  $2\pi$ . The FSR of ring 1 is  $\Omega_{\text{FSR}} = 2\pi c / (n_g L_1)$ . The FDM therefore offers an interpretation of the mode-splitting in terms of dispersion engineering, which was also employed in [6, 7]. The parameters  $\nu_n$  and  $g$  from the FDM and CMM can be related from the expressions for the frequency shift induced by the ring-ring coupling

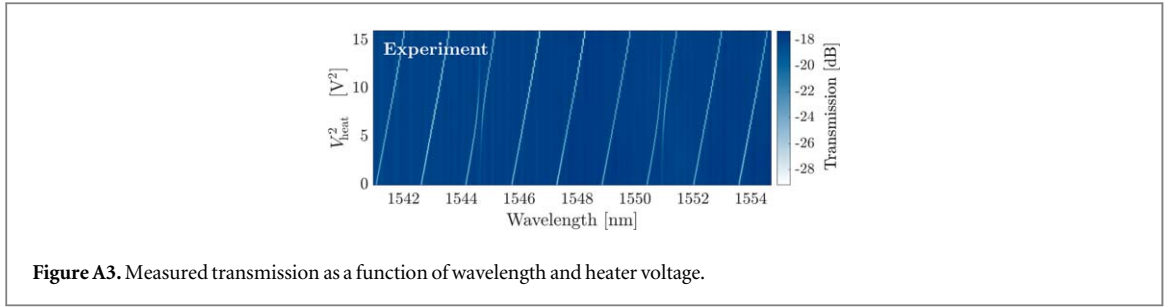


**Figure A3.** Measured transmission as a function of wavelength and heater voltage.

$$\begin{aligned} \Phi_1(\omega_{i-} + \Delta\omega) + \arg\{\bar{h}_{12}(\omega_{i-} + \Delta\omega)\} &= 2\pi p \\ \Rightarrow \frac{n_g L_1}{c} \Delta\omega + \arctan \left[ \frac{-(1 - \nu_2^2) \sin\left(\frac{n_g L_2}{c} \Delta\omega\right)}{2\nu_2 - (1 + \nu_2^2) \cos\left(\frac{n_g L_2}{c} \Delta\omega\right)} \right] &= 2\pi p, \end{aligned} \quad (\text{A18})$$

where  $\Delta\omega = \sqrt{g^2 - (\gamma_i/4)^2}$ . Figure A2(b) plots the transmission calculated from the FDM and CMM using equations (A16)–(A18) to relate the parameters. The good agreement illustrates that the CMM is a good approximation over a fairly large bandwidth close to the resonances.

The effective index,  $\tilde{n}_{\text{eff}}$ , group index,  $n_g$ , and through-coupling,  $\nu_n$ , can be calculated from mode solvers such as Lumerical or Comsol given the cross-section geometry of the waveguides. Using the CMM and FDM to relate these parameters to estimates of the device performance in equations (A4) and (A7), it is possible to design devices with specific properties.

### A.3. Interferometrically coupled ring

To analyze the properties of an interferometrically coupled ring, we introduce a transfer matrix corresponding to equation (A14) for interferometric coupling

$$C^{(\mathcal{I},n)} = e^{i\psi_R} \begin{bmatrix} \nu_n^2 - e^{i\psi} (1 - \nu_n^2) & i\nu_n \sqrt{1 - \nu_n^2} (1 + e^{i\psi}) \\ i\nu_n \sqrt{1 - \nu_n^2} (1 + e^{i\psi}) & \nu_n^2 (1 + e^{i\psi}) - 1 \end{bmatrix}. \quad (\text{A19})$$

The phase accumulated in the ring (bus waveguide) arm is  $\psi_R$  ( $\psi_B$ ) and  $\psi = \psi_B - \psi_R$ . The directional couplers are assumed identical with a through-coupling of  $\nu_n$ . Considering a case without input fields ( $s_{\text{in}} = 0$ ) and a field,  $s_g$ , being generated inside ring 1 ( $s_{1-} = C_{1,1}^{(\mathcal{I},1)} s_{1+} + s_g$ ), the solution to equation (A11) is

$$\frac{s_{1-}}{s_g} = \frac{1}{1 - \bar{C}_{1,1}^{(\mathcal{I},1)} e^{i\Phi_1} \bar{h}_{12}}, \quad (\text{A20})$$

where  $\Phi_1 = \phi_1 + \psi_R + \theta_2$  is again the round-trip phase of ring 1 without ring 2 present and  $\bar{C}^{(\mathcal{I},1)} = C^{(\mathcal{I},1)} e^{-i\psi_R}$ .

## Appendix B. Model and experiment comparison

In this section, we provide additional details on how the model parameters in table 1 are estimated. The procedure consists of fitting the measured data using the analytical expressions for transmission and frequency conversion efficiency. We use a step-wise procedure where parameters found from fitting to the transmission spectra without pump fields are used when fitting the transmission and conversion efficiency with the pumps on. The measured transmission spectrum is plotted in figure A3. To compare to the CMM only parts of the transmission spectrum in the vicinity of the three modes,  $\lambda_{i-}$ ,  $\lambda_s$ , and  $\lambda_{i+}$  is used. This is because the CMM is only a good approximation over a bandwidth in which the resonances are well-described by a Lorentzian. The ring-waveguide coupling,  $\gamma$ , is assumed equal for all modes while rings 1 and 2 are allowed different loss rates,  $\gamma_{L_1}$  and  $\gamma_{L_2}$ , respectively. Equations (10a) and (10b) then read

$$T_{i-}(\Omega) = T_{\text{cpl}}^2 \left| 1 - \frac{\gamma}{\frac{\gamma + \gamma_{L_1}}{2} - i\Omega + \frac{g^2}{\gamma_{L_2}/2 - i(\Omega - \delta_{ab})}} \right|^2, \quad (\text{A21a})$$

$$T_{i+}(\Omega) = T_{\text{cpl}}^2 \left| 1 - \frac{\gamma}{\frac{\gamma + \gamma_{L_1}}{2} - i\Omega} \right|^2. \quad (\text{A21b})$$

**Table A1.** Parameters estimated by comparison to transmission measurements without pump lasers. We only list parameters that are not included in table 1.

A	B
$-839 \times 10^9 \text{ rad s}^{-1}$	$49.9 \times 10^9 \text{ rad s}^{-1} \text{ V}^{-2}$

**Table A2.** Values of  $\delta_{\text{NL}}$  in units of  $10^9 \text{ rad s}^{-1}$  for the five data sets, estimated by fitting transmission and idler power data.

$\delta_{\text{NL}}^{(1)}$	$\delta_{\text{NL}}^{(2)}$	$\delta_{\text{NL}}^{(3)}$	$\delta_{\text{NL}}^{(4)}$	$\delta_{\text{NL}}^{(5)}$
-21.609 7	0.813 0	4.807 8	4.149 7	11.839 3

Equation (A21) includes the coupling loss,  $T_{\text{cpb}}$ , which is assumed identical for input and output grating couplers. Changing the heater voltage detunes the resonances of the two rings and we model this by letting  $\delta_{ab}$  depend on the voltage as

$$\delta_{ab} = A + BV_{\text{heat}}^2. \quad (\text{A22})$$

Fitting equation (A21) to the data in figure A3 allows us to estimate the parameters  $\gamma$ ,  $\gamma_{L_1}$ ,  $\gamma_{L_2}$ ,  $g$ ,  $A$ , and  $B$  (values for  $A$  and  $B$  are listed in table A1). The coupling loss,  $T_{\text{cpb}}$ , is estimated as the mean value of the transmission away from any resonances. When the pumps are turned on there will be a nonlinear loss in ring 1 due to free-carrier-absorption from carriers generated by TPA. This is included in equation (A21) by introducing a modified loss rate only in ring 1,  $\bar{\gamma}_{L_1} = \gamma_{L_1} + \gamma_{\text{FCA}}$ . Additionally, the resonances of ring 1 red-shift due to the heat generated by TPA. This is included by modifying  $\delta_{ab}$  as  $\Delta_{ab} = \delta_{ab} + \delta_{\text{NL}}$ . This leaves only  $\bar{\chi}$  to be determined, which is done by also fitting the converted spectra in figures 4(b)–(d) using modified versions of equations (A4) and (A7)

$$\zeta(\Omega) = \frac{4g^2}{[\gamma_{L_2} + i2(\Delta_{ab} - \Omega)](\gamma + \bar{\gamma}_{L_1} - i2\Omega)} + 1 \quad (\text{A23})$$

$$\eta_{i+}(\Omega) = \left| \frac{4\gamma\bar{\chi}}{(\gamma + \bar{\gamma}_{L_1} - i2\Omega)^2} \right|^2, \quad \eta_{i-} = \frac{1}{|\zeta|^2} \eta_{i+}. \quad (\text{A24})$$

Since the measured conversion efficiency in our experiment is much smaller than one, we make the simplifying assumption that the signal field is undepleted, which corresponds to neglecting the terms  $-i\bar{\chi}^*A_{i+} - i\bar{\chi}A_{i-}$  in equation (A3a). The parameters  $\gamma_{\text{FCA}}$ ,  $\delta_{\text{NL}}$ , and  $\bar{\chi}$  are estimated by simultaneously fitting transmission and idler output power data. Note that the parameters found from transmission data without pumps are held fixed in this process. We use five datasets corresponding to different heater settings, three of which are shown in figures 4(b)–(d). The nonlinear loss,  $\gamma_{\text{FCA}}$ , and Kerr nonlinearity,  $\bar{\chi}$ , are assumed to be identical for all five datasets whereas the nonlinear shifts,  $\delta_{\text{NL}}$ , are allowed to vary among them. This is due to the fact that the thermal locking procedure [5] used to tune the pumps into resonance does not consistently result in exactly the same resonance shift even if the pump power is identical. The values of the nonlinear shifts are listed in table A2. The nonlinearity may also be estimated based on the other parameters as well as the properties of the ring. Using the results in [38], we estimate the nonlinear coupling rate,  $\bar{\chi}$ , of our device

$$|\bar{\chi}| = \Lambda |\bar{\beta}_{p^{(2)}}^* \bar{\beta}_{p^{(1)}}|, \quad (\text{A25})$$

where the parameters on the right hand side are [38]

$$\Lambda \approx \frac{2\hbar\omega_{\text{ref}}^2 cn_2}{n_{\text{eff}}^2 V_{\text{ring}}}, \quad |\bar{\beta}_{p^{(j)}}| = 2 \frac{\sqrt{\gamma_j}}{\Gamma_j} \sqrt{\frac{P_{p_j}}{\hbar\omega_{\text{ref}}}}. \quad (\text{A26})$$

The nonlinear refractive index is  $n_2$  and  $V_{\text{ring}}$  is the volume of ring 1. Assuming both pump modes are identical to the signal mode and inserting equation (A26) into (A25) yields

$$|\bar{\chi}| = \frac{8\omega_{\text{ref}} cn_2}{n_{\text{eff}}^2 V_{\text{ring}}} \frac{\gamma_s}{\Gamma_s^2} \sqrt{P_{p_1} P_{p_2}}. \quad (\text{A27})$$

As mentioned in section 2 we measured the idler power at the up- and down-converted resonances as a function of wavelength for each setting of the signal laser wavelength,  $\lambda$ . An example of the corresponding 2D idler power maps is shown in figure A4. The dotted blue lines correspond to cross-sections with wavelengths  $(\lambda, \lambda - \lambda_{\text{FSR}})$  for the up-converted mode, and  $(\lambda, \lambda + \lambda_{\text{FSR}})$  for the down-converted mode.

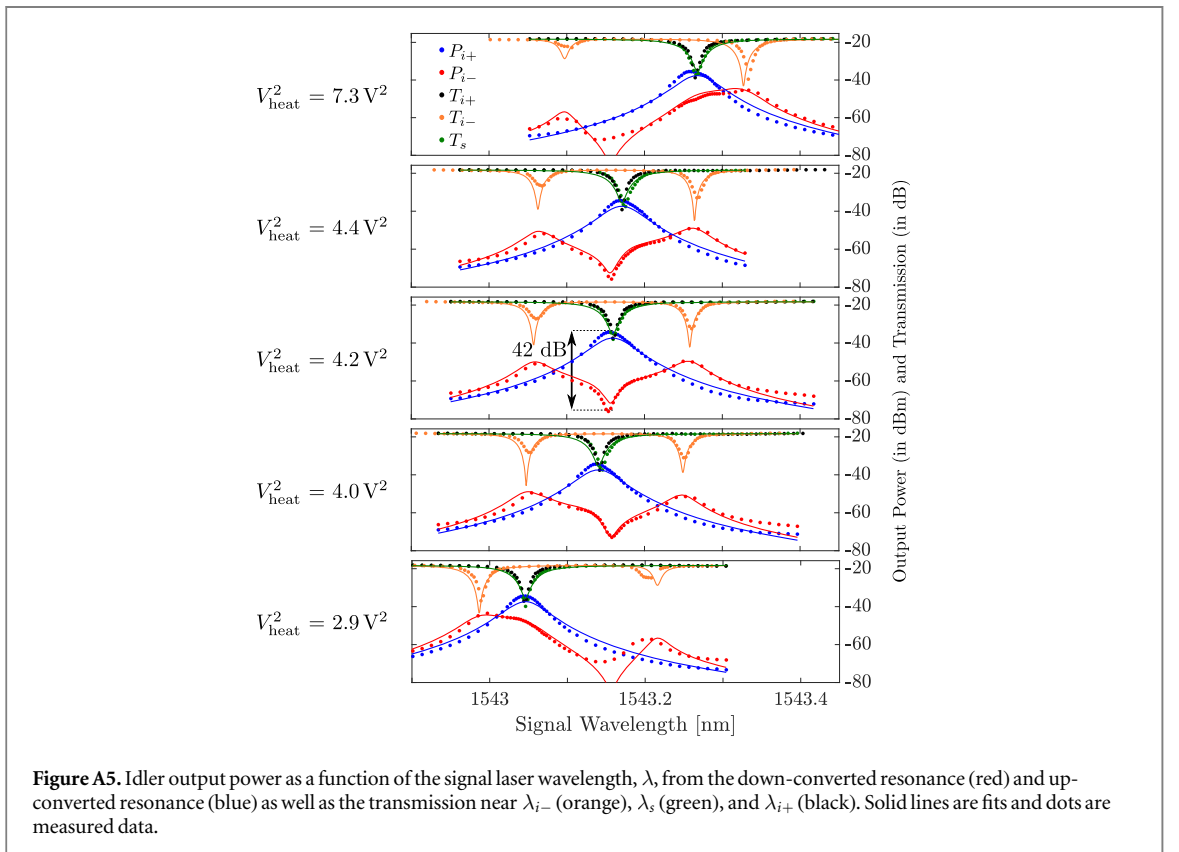
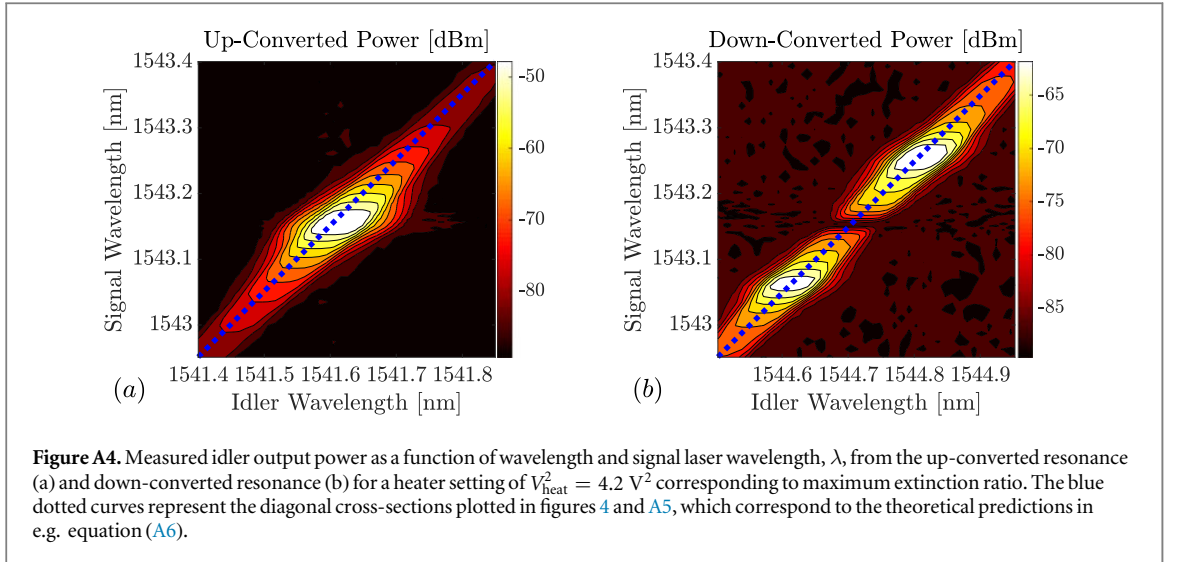


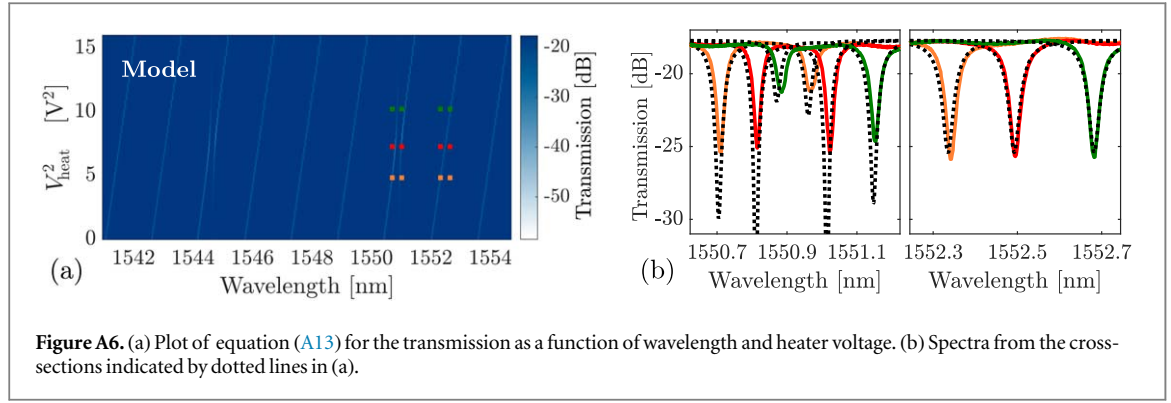
Figure A5 shows the idler power along the cross-sections for all five data sets using the values in table A2 for the fitted curves. A good qualitative agreement between measurement and model predictions is observed for all five data sets.

### B.1. Fitting using FDM

As an additional check of the fitted parameters using the CMM, we also use the FDM to fit the spectra in figure A3. Here, we use the entire wavelength range of the measurement as the FDM models all the resonances as well as the FSR of the rings. Equation (A13) is used to estimate the parameters  $\nu_1$ ,  $\nu_2$ ,  $\tilde{n}_{\text{eff}}$ , and  $n_g$ . We assume only the real part of  $\tilde{n}_{\text{eff}}$  changes with applied voltage as in equation (A22)

$$n'_{\text{eff}}(V_{\text{heat}}) = n'_0 + \partial n_V V_{\text{heat}}^2. \quad (\text{A28})$$



**Table A3.** FDM fitting parameters.

$\gamma = 28 \times 10^9 \text{ rad s}^{-1}$	$\gamma_{L_1} = 12 \times 10^9 \text{ rad s}^{-1}$
$g = 80 \times 10^9 \text{ rad s}^{-1}$	$\gamma_{L_2} = 23 \times 10^9 \text{ rad s}^{-1}$
$n'_0 = 2.618$	$n_g = 4.73$
$\partial n_V = 1.96 \times 10^{-4} \text{ V}^{-2}$	

The proportionality constant is

$$\partial n_V = \frac{1}{R} \frac{\partial n}{\partial T} \frac{\partial T}{\partial U}, \quad (\text{A29})$$

where  $R$  is the resistance of the titanium wire,  $\partial U / \partial T$  is its heat capacity, and  $\partial n / \partial T$  is the thermo-optic coefficient of silicon. Figure A6(a) shows a comparison with figure A3 using the fitting parameters listed in table A3. The largest discrepancy is observed for heater voltages where the resonances of the rings align. However, when ring 1 is either red- or blue-detuned from ring 2, the agreement is better as observed in figure A6(b). The model agrees well with the measurement data at frequencies close to modes of ring 1 that are far-detuned from modes of ring 2, which is also observed from figure A6(b). The values of parameters in table A3 agree well with those in table 1, which provides additional confidence in our parameter estimation.

## Appendix C. Cascaded FWM

To consider the effect of first-order cascaded BS-FWM processes we introduce an extra mode  $A_{i++}$  that couples to  $A_{i+}$

$$\dot{A}_s = -\frac{\Gamma_s}{2} A_s - i\bar{\chi}^* A_{i+} - i\bar{\chi} A_{i-} - \sqrt{\gamma_s} S_{in,s} \quad (\text{A30a})$$

$$\dot{A}_{i+} = -\frac{\Gamma_i}{2} A_{i+} - i\bar{\chi} A_s - i\bar{\chi}^* A_{i++} \quad (\text{A30b})$$

$$\dot{A}_{i++} = -\frac{\Gamma_i}{2} A_{i++} - i\bar{\chi} A_{i+} \quad (\text{A30c})$$

$$\dot{A}_{i-} = -\frac{\Gamma_i}{2} A_{i-} - i\bar{\chi}^* A_s - igB \quad (\text{A30d})$$

$$\dot{B} = \left( -i\delta_{ab} - \frac{\gamma_L}{2} \right) B - igA_{i-} \quad (\text{A30e})$$

$$S_{out,j} = S_{in,j} + \sqrt{\gamma_j} A_j, \quad j \in \{s, i-, i+, i++\}. \quad (\text{A30f})$$

Again, we have assumed that all idler modes have the same coupling rates. For  $\delta_{ab} = 0$  and  $\Omega = 0$ , we find the extinction ratio

$$\zeta = \frac{\Gamma_i^2 (4G^2 + 1)}{\Gamma_i^2 + 4\bar{\chi}^2}. \quad (\text{A31})$$

The up-conversion efficiency is

$$\eta_{i+} = \left| \frac{4\sqrt{\gamma_i\gamma_s}\bar{\chi}}{\Gamma_i\Gamma_s + 4\bar{\chi}^2\left(1 + \frac{\Gamma_s}{\Gamma_i} + \zeta^{-1}\right)} \right|^2. \quad (\text{A32})$$

For  $\zeta \gg 1$ , the maximum conversion efficiency is

$$\eta_{i+}^{\max} = \frac{\gamma_i\gamma_s}{\Gamma_s(\Gamma_i + \Gamma_s)} \quad (\text{A33})$$

which is achieved with a nonlinearity given by

$$\chi^{\max} = \frac{1}{2}\Gamma_i\sqrt{\frac{\Gamma_s}{\Gamma_i + \Gamma_s}}. \quad (\text{A34})$$

Inserting equation (A34) into (A31) yields

$$\zeta^{\max} = (4G^2 + 1)\frac{\Gamma_i + \Gamma_s}{\Gamma_i + 2\Gamma_s}. \quad (\text{A35})$$

From equations (A31)–(A35) it is seen that the additional requirement  $\Gamma_i \gg \Gamma_s$  must be imposed to reach near-unity conversion efficiency when taking cascaded processes into account. In fact, equation (A33) shows that the conversion efficiency is limited to 50% if  $\gamma_i = \gamma_s$ . This number would be even lower when considering second- and higher-order cascaded processes.

## Appendix D. Spectral correlations

The joint state of a photon pair created at  $\omega_{s,0}$  and  $\omega_{i,0}$  after they exit the resonator is

$$|\Psi\rangle = \iint d\Omega_i d\Omega_s \mathcal{A}(\Omega_s, \Omega_i) \hat{\phi}_s^\dagger(\Omega_s) \hat{s}_i^\dagger(\Omega_i) |0_s\rangle |0_i\rangle, \quad (\text{A36})$$

where  $\hat{s}_i^\dagger(\Omega_i)$  creates a photon in the waveguide at the frequency  $\omega = \omega_{i,0} + \Omega_i$ . Since  $\gamma_s = 0$ , the signal photon only couples to the environment and  $\hat{\phi}_s^\dagger(\Omega_s)$  is therefore the creation operator for heat bath modes at  $\omega = \omega_{s,0} + \Omega_s$ . The joint spectral amplitude (JSA),  $\mathcal{A}(\Omega_s, \Omega_i)$ , is essentially a two-dimensional wave function containing information about the distribution and correlations of the signal and idler frequencies. For photons created in a resonator, the JSA is proportional to [17, 28]

$$\mathcal{A}(\Omega_s, \Omega_i) = F_p(\Omega_s + \Omega_i) l_i(\Omega_i) l_s(\Omega_s), \quad (\text{A37})$$

where  $l_j(\Omega_j) = [\Gamma_j/2 + i\Omega_j]^{-1}$  are Lorentzian lineshapes with a width determined by  $\Gamma_j$  with  $j \in \{s, i, p\}$ . The pump function  $F_p$  is given by

$$F_p(\Omega) = \int d\Omega' A_p(\Omega - \Omega') l_p(\Omega - \Omega') A_p(\Omega') l_p(\Omega'), \quad (\text{A38})$$

which is a convolution of the pump field in the ring,  $A_p(\Omega) l_p(\Omega)$ , with itself. The JSA may be expanded using a Schmidt decomposition

$$\mathcal{A}(\Omega_s, \Omega_i) = \sum_k \lambda_k \psi_{i,k}(\Omega_i) \psi_{s,k}(\Omega_s), \quad (\text{A39})$$

where  $\psi_{j,k}$ ,  $j \in \{s, i\}$  are orthonormal signal and idler Schmidt modes and  $\lambda_k$  the Schmidt coefficients. The square of the signal density matrix (originating from a partial trace of the joint state operator over the idler sub-space) is used to define the spectral purity of heralded photons [29]

$$P = \sum_k \lambda_k^4. \quad (\text{A40})$$

All information about signal-idler frequency correlations are contained in  $F_p(\Omega_s + \Omega_i)$  as seen from equation (A37). The maximum spectral purity is achieved when the spectral width of the pump pulse is much larger than the width of the pump mode and the approximation  $A_p \approx 1$  can be made in equation (A38).

## Appendix E. Shaping output photons

The temporal shape of emitted photons is controllable via the time-dependent BS-FWM coupling terms in equation (A3). To determine the function,  $\bar{\chi}_{\text{in}}(t)$ , giving rise to a specific output, we consider the equations of motion for an interferometrically coupled device

$$\dot{A}_o = -\frac{\Gamma_o}{2}A_o - i\bar{\chi}_{in}^*A_s - \sqrt{\gamma_o}S_{in,o} \quad (\text{A41a})$$

$$\dot{A}_s = -\frac{\gamma_L}{2}A_s - i\bar{\chi}_{in}A_o \quad (\text{A41b})$$

$$S_{out,o} = S_{in,o} + \sqrt{\gamma_o}A_o. \quad (\text{A41c})$$

For simplicity we consider only two modes (corresponding to the limit of large  $G$ ), the signal ( $s$ ) and output ( $o$ ). Instead of considering how to emit a function  $S_{out,o}(t)$  in the absence of any inputs ( $S_{in,o} = 0$ ), we consider how to absorb a function  $S_{in,o}(-t) = S_{out,o}(t)$ . If  $\bar{\chi}_{in}(t)$  is the control function that enables absorption of  $S_{in,o}(-t)$ , then  $\bar{\chi}_{out}(t) = \bar{\chi}_{in}(-t)$  is the control function that enables emission of  $S_{out,o}(t)$  (in the limit of zero loss). Determining  $\bar{\chi}_{in}(t)$  therefore solves both the absorption and emission problem.

To fully absorb a pulse into the resonator, we must have  $S_{out,o} = 0$  in equation (A41c) and therefore  $A_o = -S_{in,o}/\sqrt{\gamma_o}$ . Inserting into equation (A41a) yields

$$\dot{S}_{in,o} = -\frac{\Gamma_o}{2}S_{in,o} + i\bar{\chi}_{in}^*\sqrt{\gamma_o}A_s + \gamma_o S_{in,o} \Rightarrow \dot{S}_{in,o} - \frac{\gamma_o - \gamma_L}{2}S_{in,o} = i\bar{\chi}_{in}^*\sqrt{\gamma_o}A_s. \quad (\text{A42})$$

The solution for  $A_s$  is found by rearranging terms in equation (A41b)

$$\frac{d}{dt}(A_s e^{\frac{\gamma_L}{2}t}) e^{-\frac{\gamma_L}{2}t} = i\frac{\bar{\chi}_{in}}{\sqrt{\gamma_o}}S_{in,o} \Rightarrow A_s = \frac{ie^{-\frac{\gamma_L}{2}t}}{\sqrt{\gamma_o}} \int_0^t e^{\frac{\gamma_L}{2}t'} \bar{\chi}_{in}(t') S_{in,o}(t') dt'. \quad (\text{A43})$$

Inserting the result for  $A_s$  into equation (A42) we find

$$\left(\frac{\gamma_o - \gamma_L}{2}S_{in,o} - \dot{S}_{in,o}\right) S_{in,o} e^{\gamma_L t} = \bar{\chi}_{in}^* e^{\frac{\gamma_L}{2}t} S_{in,o} \int_0^t e^{\frac{\gamma_L}{2}t'} \bar{\chi}_{in}(t') S_{in,o}(t') dt'. \quad (\text{A44})$$

We assume  $S_{in,o} \in \mathbb{R}$  such that the RHS can be written as

$$(x - iy) \int (x + iy) = x \int x + y \int y + i(x \int y - y \int x), \quad (\text{A45})$$

where the functions are given by  $x = \text{Re}\{\bar{\chi}_{in}\} S_{in,o} \exp(\gamma_L t/2)$  and similarly  $y = \text{Im}\{\bar{\chi}_{in}\} S_{in,o} \exp(\gamma_L t/2)$ . By defining the functions

$$X = \int x = R \cos(\theta), \quad Y = \int y = R \sin(\theta), \quad (\text{A46})$$

the real part of equation (A45) can be rewritten as

$$\dot{X}X + \dot{Y}Y = [\dot{R}\cos(\theta) - R\sin(\theta)\dot{\theta}]R\cos(\theta) + [\dot{R}\sin(\theta) + R\cos(\theta)\dot{\theta}]R\sin(\theta) = \dot{R}R = \frac{1}{2} \frac{d}{dt}(R^2). \quad (\text{A47})$$

The imaginary part of equation (A45) is

$$\dot{X}Y - \dot{Y}X = [\dot{R}\cos(\theta) - R\sin(\theta)\dot{\theta}]R\sin(\theta) - [\dot{R}\sin(\theta) + R\cos(\theta)\dot{\theta}]R\cos(\theta) = -R^2\dot{\theta}. \quad (\text{A48})$$

Since  $S_{in,o}$  is real, we can define a real function

$$f_o = \left(\frac{\gamma_o - \gamma_L}{2}S_{in,o} - \dot{S}_{in,o}\right) S_{in,o} e^{\gamma_L t}, \quad (\text{A49})$$

such that the solution to equations (A47) and (A48) are

$$R(t) = \sqrt{2 \int_0^t f_o(s) ds} \quad (\text{A50})$$

$$\dot{\theta} = 0 \Rightarrow \theta = C_1, \quad (\text{A51})$$

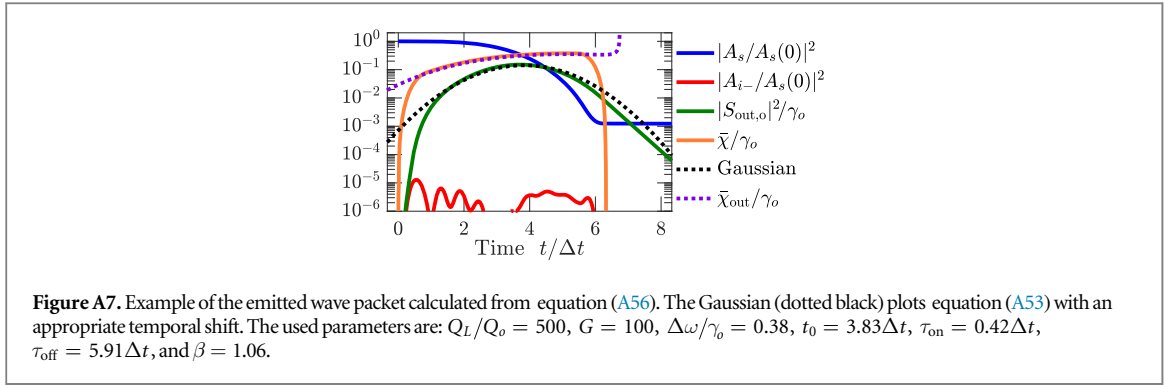
where  $C_1$  is an arbitrary real constant. For simplicity we could choose  $C_1 = 0$ , such that  $X = R$  and therefore

$$\bar{\chi}_{in} S_{in,o} e^{\frac{\gamma_L}{2}t} = \dot{R} = \frac{f_o}{\sqrt{2 \int f_o}} \Rightarrow \bar{\chi}_{in} = \frac{f_o e^{-\frac{\gamma_L}{2}t}}{S_{in,o} \sqrt{2 \int f_o}}. \quad (\text{A52})$$

### E.1. Gaussian wave packet

Having determined the general solution in equation (A52), we now consider a specific example of a Gaussian wave packet

$$S_{in,o}(t) = \sqrt{\frac{2}{\Delta t}} \left(\frac{\ln(2)}{\pi}\right)^{\frac{1}{4}} \exp\left(-2 \ln(2) \frac{t^2}{\Delta t^2}\right), \quad (\text{A53})$$



with a FWHM temporal width  $\Delta t$  and spectral width  $\Delta\omega = 4 \ln(2)/\Delta t$ . First, we note that equation (A52) is only a solution if the anti-derivative of  $f_o$  is positive. For the Gaussian wave packet in equation (A53) we have

$$\dot{S}_{in,o} = -\frac{4 \ln(2)}{\Delta t^2} t S_{in,o} = -\frac{\Delta\omega}{\Delta t} t S_{in,o}. \quad (\text{A54})$$

Since  $S_{in,o}$  is positive, the condition for  $f_o$  to be positive is

$$f_o \geq 0 \Rightarrow \frac{\gamma_o - \gamma_L}{2} + \frac{\Delta\omega}{\Delta t} t \geq 0 \Rightarrow \frac{t}{\Delta t} \geq -\frac{1}{2} \frac{\gamma_o}{\Delta\omega} \left(1 - \frac{\gamma_L}{\gamma_o}\right). \quad (\text{A55})$$

This means  $f_o$  is negative in the leading part of the wave packet up until the time given by equation (A55) and the solution for  $\bar{\chi}_{in}$  is invalid. However, this critical time can be pushed arbitrarily far into the tail of the Gaussian by increasing the coupling rate of the output mode,  $\gamma_o$ , relative to the pulse bandwidth,  $\Delta\omega$ .

To calculate the emission efficiency in the presence of loss and the down-converted mode, we consider the equations of motion

$$\dot{A}_o = -\frac{\Gamma_o}{2} A_o - i\bar{\chi}_{out} A_s \quad (\text{A56a})$$

$$\dot{A}_s = -\frac{\gamma_L}{2} A_s - i\bar{\chi}_{out} A_o - i\bar{\chi}_{out} A_{i-} \quad (\text{A56b})$$

$$\dot{A}_{i-} = -\frac{\Gamma_o}{2} A_{i-} - i\bar{\chi}_{out} A_s - igB \quad (\text{A56c})$$

$$\dot{B} = \left(-i\delta_{ab} - \frac{\gamma_L}{2}\right) B - igA_{i-} \quad (\text{A56d})$$

$$S_{out,o} = \sqrt{\gamma_o} A_o. \quad (\text{A56e})$$

For simplicity, we assume the down-converted mode and output mode have the same coupling rates. The appropriate initial condition is  $A_s(0) = 1$ ,  $A_o(0) = A_{i-}(0) = B(0) = 0$ , and  $\bar{\chi}_{out}(0) = 0$ . This corresponds to a signal photon occupying mode  $A_s$  and the BS-FWM pumps not having entered the resonator yet. The absolute square of the cavity fields then correspond to the probability of the photon occupying these modes,  $\mathcal{P}(j) = |A_j|^2$ . As mentioned above, the solution for  $\bar{\chi}_{out}(t)$  is given by equation (A52) evaluated at  $-t$ . It turns out to be advantageous to multiply  $\bar{\chi}_{out}$  by an envelope function,  $F_{env}(t) = f_{env}(t - \tau_{on}) \times f_{env}(\tau_{off} - t)$ , due to loss and the divergence in  $\bar{\chi}_{in}$ . The sides of the envelope are

$$f_{env}(t) = \left[ 1 + \frac{1 + \sin\left(\frac{\pi t}{\tau_{env}}\right)}{2} \theta\left(t + \frac{\tau_{env}}{2}\right) \right] \theta\left(t - \frac{\tau_{env}}{2}\right), \quad (\text{A57})$$

where  $\theta(t)$  is a step function that equals one when  $t > 0$  and zero otherwise. The envelope rises from zero to one in the interval  $t \in [-\tau_{env}/2, \tau_{env}/2]$  as half a period of the sine function. Figure A7 shows an example of the solution to equation (A56) along with the BS-FWM pump function given by  $\bar{\chi} = \beta \bar{\chi}_{out} F_{env}$ . The amplitude,  $\beta > 1$ , is used to ensure that the entire population in  $A_s$  may be converted to  $A_o$  despite the reduction in area under the orange curve resulting from multiplication by  $F_{env}$ . The function  $\bar{\chi}$  (orange curve in figure A7) is found by optimizing  $\tau_{on}$ ,  $\beta$ , and  $\Delta\omega/\gamma_o$  to maximize  $\eta_{out}$  for a fixed  $G$  and  $Q_L/Q_o$  under the constraint that  $OL \geq 99\%$ . The cutoff time,  $\tau_{off}$ , is fixed for a given pulse width,  $\Delta\omega$ , to avoid the divergence in  $\bar{\chi}_{out}$  (occurring at  $t \approx 7\Delta t$  in figure A7).

## ORCID iDs

Mikkel Heuck  <https://orcid.org/0000-0001-9769-6005>

Jacob Gade Koefoed  <https://orcid.org/0000-0001-6056-4674>

## References

- [1] Leuthold J, Koos C and Freude W 2010 Nonlinear silicon photonics *Nat. Photon.* **4** 535–44
- [2] McKinstrie C J, Harvey J D, Radic S and Raymer M G 2005 Translation of quantum states by four-wave mixing in fibers *Opt. Express* **13** 9131
- [3] Kumar P 1990 Quantum frequency conversion *Opt. Lett.* **15** 1476
- [4] Willner A E, Yilmaz O F, Wang J, Wu X, Bogoni A, Zhang L and Nuccio S R 2011 Optically efficient nonlinear signal processing *IEEE J. Sel. Top. Quantum Electron.* **17** 320–2
- [5] Li Q, Davanco M and Srinivasan K 2016 Efficient and low-noise single-photon-level frequency conversion interfaces using silicon nanophotonics *Nat. Photon.* **10** 406–15
- [6] Gentry C M, Zeng X and Popović M A 2014 Tunable coupled-mode dispersion compensation and its application to on-chip resonant four-wave mixing *Opt. Lett.* **39** 5689
- [7] Xue X, Xuan Y, Wang P H, Liu Y, Leaird D E, Qi M and Weiner A M 2015 Normal-dispersion microcombs enabled by controllable mode interactions *Laser Photonics Rev.* **9** L23–8
- [8] Clemmen S, Farsi A, Ramelow S and Gaeta A L 2016 Ramsey interference with single photons *Phys. Rev. Lett.* **117** 223601
- [9] Joshi C, Farsi A, Clemmen S, Ramelow S and Gaeta A L 2018 Frequency multiplexing for quasi-deterministic heralded single-photon sources *Nat. Commun.* **9** 847
- [10] Migdall A L, Branning D and Castelletto S 2002 Tailoring single-photon and multiphoton probabilities of a single-photon on-demand source *Phys. Rev. A* **66** 053805
- [11] Collins M J et al 2013 Integrated spatial multiplexing of heralded single-photon sources *Nat. Commun.* **4** 2582
- [12] Kaneda F, Christensen B G, Wong J J, McCusker K T, Park H S and Kwiat P G 2015 A time-multiplexed heralded single-photon source *Optica* **2** 1010–3
- [13] Bonneau D, Mendoza G J, O'Brien J L and Thompson M G 2015 Effect of loss on multiplexed single-photon sources *New J. Phys.* **17** 043057
- [14] Mendoza G J, Santagati R, Munns J, Hemsley E, Piekarek M, Martín-López E, Marshall G D, Bonneau D, Thompson M G and O'Brien J L 2016 Active temporal and spatial multiplexing of photons *Optica* **3** 127
- [15] Grimau Puigibert M, Aguilar G H, Zhou Q, Marsili F, Shaw M D, Verma V B, Nam S W, Oblak D and Tittel W 2017 Heralded single photons based on spectral multiplexing and feed-forward control *Phys. Rev. Lett.* **119** 1–6
- [16] Kues M et al 2017 On-chip generation of high-dimensional entangled quantum states and their coherent control *Nature* **546** 622–6
- [17] Vernon Z et al 2017 Truly unentangled photon pairs without spectral filtering *Opt. Lett.* **42** 3638–41
- [18] Ding Y, Peucheret C and Ou H 2013 Ultra-high-efficiency apodized grating coupler using a fully etched photonic crystal *Opt. Lett.* **38** 2732–4
- [19] Reithmaier J P, Sek G, Löffler A, Hofmann C, Kuhn S, Reitzenstein S, Keldysh L V, Kulakovskii V D, Reinecke T L and Forchel A 2004 Strong coupling in a single quantum dot-semiconductor microcavity system *Nature* **432** 197–200
- [20] Madsen C K, Lenz G, Bruce A J, Cappuzzo M A, Gomez L T and Scotti R E 1999 Integrated all-pass filters for tunable dispersion and dispersion slope compensation *IEEE Photonics Technol. Lett.* **11** 1623–5
- [21] Heuck M, Pant M and Englund D 2018 Temporally and spectrally multiplexed single photon source using quantum feedback control for scalable photonic quantum technologies *New J. Phys.* **20** 063046
- [22] Sacher W D, Huang Y, Lo G Q and Poon J K S 2015 Multilayer silicon nitride-on-silicon integrated photonic platforms and devices *J. Lightwave Technol.* **33** 901–10
- [23] Shainline J M, Buckley S M, Nader N, Gentry C M, Cossel K C, Cleary J W, Popović M, Newbury N R, Nam S W and Mirin R P 2017 Room-temperature-deposited dielectrics and superconductors for integrated photonics *Opt. Express* **25** 10322
- [24] Gehl M, Long C, Trotter D, Starbuck A, Pomerene A, Wright J B, Melgaard S, Siirola J, Lentine A L and DeRose C 2017 Operation of high-speed silicon photonic micro-disk modulators at cryogenic temperatures *Optica* **4** 374
- [25] Timurdogan E, Poulton C V, Byrd M J and Watts M R 2017 Electric field-induced second-order nonlinear optical effects in silicon waveguides *Nat. Photon.* **11** 200–6
- [26] Gentry C M, Magana-Loaiza O S, Wade M T, Pavanello F, Gerrits T, Lin S, Shainline J M, Dyer S D, Nam S W, Mirin R P and Popovic M A 2018 Monolithic source of entangled photons with integrated pump rejection *Conf. on Lasers and Electro-Optics, JThAC.3* pp 3–4
- [27] McCaughan A N and Berggren K K 2014 A superconducting-nanowire three-terminal electrothermal device *Nano Lett.* **14** 5748–53
- [28] Helt L G, Yang Z, Liscidini M and Sipe J E 2010 Spontaneous four-wave mixing in microring resonators *Opt. Lett.* **35** 3006–8
- [29] Christensen J B, Koefoed J G, Rottwitt K and McKinstrie C 2018 Engineering spectrally unentangled photon pairs from nonlinear microring resonators by pump manipulation *Opt. Lett.* **43** 859–62
- [30] Nysteen A, McCutcheon D P S, Heuck M, Mørk J and Englund D R 2017 Limitations of two-level emitters as nonlinearities in two-photon controlled-PHASE gates *Phys. Rev. A* **95** 1–7
- [31] Brańczyk A M 2017 Hong-Ou-Mandel interference 1–17 arXiv
- [32] Pruessner M W, Park D, Stievater T H, Kozak D A and Rabinovich W S 2016 Broadband opto-electro-mechanical effective refractive index tuning on a chip *Opt. Express* **24** 13917
- [33] Christ A and Silberhorn C 2012 Limits on the deterministic creation of pure single-photon states using parametric down-conversion *Phys. Rev. A* **85** 1–6
- [34] Okawachi Y, Saha K, Levy J S, Wen Y H, Lipson M and Gaeta A L 2011 Octave-spanning frequency comb generation in a silicon nitride chip *Opt. Lett.* **36** 3398–400
- [35] Ji X, Barbosa F A S, Roberts S P, Dutt A, Cardenas J, Okawachi Y, Bryant A, Gaeta A L and Lipson M 2017 Ultra-low-loss on-chip resonators with sub-milliwatt parametric oscillation threshold *Optica* **4** 619
- [36] Combes J, Kerckhoff J and Sarovar M 2017 The SLH framework for modeling quantum input-output networks *Adv. Phys. X* **6149** 784–888
- [37] Vernon Z and Sipe J E 2015 Spontaneous four-wave mixing in lossy microring resonators *Phys. Rev. A* **91** 1–9
- [38] Vernon Z, Liscidini M and Sipe J E 2016 Quantum frequency conversion and strong coupling of photonic modes using four-wave mixing in integrated microresonators *Phys. Rev. A* **94** 1–14